

SPECIAL ISSUE PAPER - NUMERICAL METHODS AND APPLICATIONS OF
MULTI-PHYSICS IN BIOMECHANICAL MODELING

Computational modeling of chemo-electro-mechanical coupling:
A novel implicit monolithic finite element approach

J. Wong¹, S. Göktepe² and E. Kuhl^{3,*},[†]

¹*Department of Mechanical Engineering, Stanford University, Stanford, CA 94305, U.S.A.*

²*Department of Civil Engineering, Middle East Technical University, 06800 Ankara, Turkey*

³*Departments of Mechanical Engineering, Bioengineering and Cardiothoracic Surgery, Stanford University, Stanford, CA 94305, U.S.A.*

SUMMARY

Computational modeling of the human heart allows us to predict how chemical, electrical, and mechanical fields interact throughout a cardiac cycle. Pharmacological treatment of cardiac disease has advanced significantly over the past decades, yet it remains unclear how the local biochemistry of an individual heart cell translates into global cardiac function. Here, we propose a novel, unified strategy to simulate excitable biological systems across three biological scales. To discretize the governing chemical, electrical, and mechanical equations in space, we propose a monolithic finite element scheme. We apply a highly efficient and inherently modular global–local split, in which the deformation and the transmembrane potential are introduced globally as nodal degrees of freedom, whereas the chemical state variables are treated locally as internal variables. To ensure unconditional algorithmic stability, we apply an implicit backward Euler finite difference scheme to discretize the resulting system in time. To increase algorithmic robustness and guarantee optimal quadratic convergence, we suggest an incremental iterative Newton–Raphson scheme. The proposed algorithm allows us to simulate the interaction of chemical, electrical, and mechanical fields during a representative cardiac cycle on a patient-specific geometry, robust and stable, with calculation times on the order of 4 days on a standard desktop computer. Copyright © 2013 John Wiley & Sons, Ltd.

Received 9 September 2012; Revised 7 February 2013; Accepted 12 April 2013

KEY WORDS: multifield; multiscale; finite element method; electrochemistry; electromechanics

1. MOTIVATION

Pharmacological treatment has opened new avenues for managing various types of cardiac disease. On a daily basis, cardiologists now prescribe antiarrhythmic agents to control heart rhythm disorders such as atrial fibrillation, atrial flutter, ventricular tachycardia, and ventricular fibrillation [1]. Although the pharmacological control of the electrical activity of the heart is reasonably well-understood, the pharmacological manipulation of the mechanical activity of the heart remains severely understudied. This is an important problem in heart failure [2], a disease associated with an annual health care cost of more than \$30 billion in the USA alone [3]. To understand how a new drug affects the interaction between chemical, electrical, and mechanical fields, systematic drug testing is of incredible clinical importance [4]. Not surprisingly, it covers a huge market ranging from single cell testing using patch clamp electrophysiology [5, 6] via cell culture testing using microelectroarray recordings [7, 8] to large animal experiments [9, 10]. Although the pharmacological manipulation of chemo-electro-mechanical coupling is relatively well-understood on the

*Correspondence to: Ellen Kuhl, 496 Lomita Mall, Durand 217, Stanford, CA 94305, U.S.A..

[†]E-mail: ekuhl@stanford.edu

single cell level [11, 12], little is known whether or not this knowledge translates into clinically relevant function on the organ level [13]. This knowledge gap presents a tremendous opportunity for quantitative, predictive computational modeling [14]. Most importantly, the nature of coupling between the underlying chemical, electrical, and mechanical fields is ideally tailored for finite element simulations, a circumstance that has been largely overlooked until today.

The first model to quantitatively characterize the electrical activity of excitable cells was the Nobel-price winning Hodgkin–Huxley model introduced more than half a century ago [15]. Initially designed for nerve cells [16, 17], the model was soon adopted for other cell types, such as pacemaker cells [18], Purkinje fiber cells [19], atrial cells [20], and ventricular cells [21–23] of the heart. Originally proposed for single cells, these approaches were generalized to multiple cells, tissues, and organs by adding a phenomenological flux term to characterize the propagation of the excitation wave. Traditionally, simulations of propagating electrical signals were dominated by biophysicists and electrical engineers [24, 25]. Their models were based on simple straightforward algorithms, discretized in space using finite differences and discretized in time using explicit time-stepping schemes [26]. To compensate for the lack of sophistication in algorithmic design, these initial models generally use a high spatial and temporal resolution, small grids and small time steps. Not surprisingly, these initial methods are extremely expensive from a computational point of view [27].

Within the past decade, physiological function has become a key focus in cardiac simulations [28], paving the way for mechanical models and finite element methods [29, 30]. However, progress was dampened by the finite difference nature of existing algorithms, making it virtually impossible to integrate mechanical deformation, in particular in the context of finite strains. The first generation of electromechanical heart models combined previously established finite difference-based electrical algorithms with finite element-based mechanical algorithms [31]. Most versions of these models are coupled unidirectionally, that is, the algorithm first calculates the electrical field and then uses it as an input to calculate the mechanical field. The advantage of this approach is that it allows us to combine different spatial and temporal resolutions for both fields [32, 33]. For loosely coupled problems, these algorithms typically perform sufficiently well [34], although we cannot really quantify the loss of information and the possible energy blow-up associated with the explicit discretization of the coupling terms. For strongly coupled problems, these algorithms require an extremely fine spatial and temporal resolution, especially during the rapid upstroke phase when all fields undergo rapid changes. To eliminate potential algorithmic instabilities, revised versions of these models are coupled bidirectionally, that is, they iterate between electrical and mechanical fields. It is not surprising that those algorithms, which integrate more information about the nature of coupling upfront have enhanced stability and performance properties [35].

Here, we challenge existing excitation–contraction algorithms and propose a second generation of chemo-electro-mechanical heart models, algorithmically redesigned from scratch. We propose a

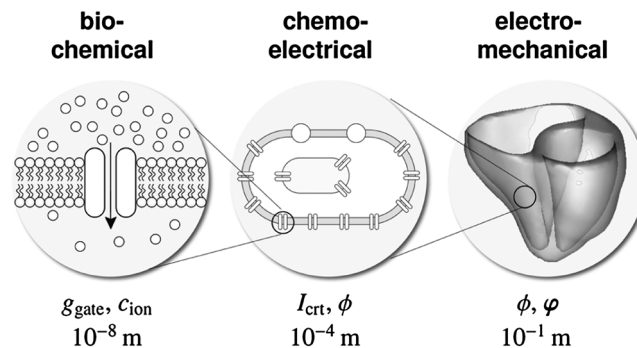


Figure 1. Multiscale model of the human heart. At the molecular level, gating variables g_{gate} and ion concentrations c_{ion} characterize the biochemical response. At the cellular level, ionic currents I_{crit} and the transmembrane potential ϕ characterize the chemo-electrical response. At the organ level, the propagation of the electrical potential ϕ and the deformation φ characterize the electromechanical response.

novel unified algorithm, which is entirely finite element based, fully coupled, monolithic, implicitly time-integrated, and consistently linearized [36]. This allows us to use existing finite element infrastructures, such as simple, ad hoc adaptive time-stepping schemes [37]. In designing our new algorithm, we take advantage of the multiscale nature of the underlying problem illustrated in Figure 1 and discretize all chemical unknowns locally on the integration point level and all electrical and mechanical unknowns globally on the node point level [38–40]. In Section 2, we summarize the underlying kinematic, balance, and constitutive equations for chemo-electro-mechanical problems. In Section 3, we then illustrate their temporal and spatial discretizations. We introduce the global system of equations, which we solve using an incremental iterative Newton–Raphson strategy. In Section 4, we specify the constitutive equations for the electrical and mechanical source and flux terms, which naturally introduce the coupling between the underlying chemical, electrical, and mechanical fields. In Section 5, we illustrate the features of the proposed model, first, locally at the single cell level, then globally for the model problem of a flat square panel and then globally at the whole heart level. We conclude with a discussion and a brief outlook in Section 6.

2. CONTINUOUS PROBLEM OF CHEMO-ELECTRO-MECHANICS

In this section, we summarize the generic continuous equations of chemo-electro-mechanical coupling characterized through a set of partial differential equations for the electrical and mechanical problems and through a system of ordinary differential equations for the chemical problem. The primary unknowns of the electrical and mechanical problems are the transmembrane potential ϕ and the deformation φ . The unknowns of the chemical problem are the local state variables, which we collectively summarize in the vector \mathbf{q} . For simple two-parameter model, \mathbf{q} would only contain a single variable, the phenomenological recovery variable r . For more sophisticated ionic models, \mathbf{q} contains a set of gating variables g_{gate} and a set of ion concentrations c_{ion} , which, at any point in time, characterize the local ionic currents I_{ct} .

2.1. Kinematic equations

To characterize the kinematic state of the body under consideration, we introduce the nonlinear deformation φ that maps particles from the undeformed reference configuration \mathcal{B}_0 at time t_0 to the deformed current configuration \mathcal{B}_t at time $t \in \mathbb{R}$,

$$\mathbf{x} = \varphi(\mathbf{X}, t) : \mathcal{B}_0 \times \mathbb{R} \rightarrow \mathcal{B}_t. \quad (1)$$

In what follows, $\{\dot{\circ}\} = d_t\{\circ\}|_X$ and $\nabla\{\circ\} = d_X\{\circ\}|_t$ denote the material time derivative and the material gradient of a quantity $\{\circ\}$. Accordingly, $\text{Div}\{\circ\} = \nabla\{\circ\} : \mathbf{I}$ denotes the material divergence, where \mathbf{I} is the second-order identity tensor. With these definitions, we can introduce the deformation gradient \mathbf{F} as the linear tangent map from the material tangent space $T\mathcal{B}_0$ to the spatial tangent space $T\mathcal{B}_t$,

$$\mathbf{F} = \nabla\varphi(\mathbf{X}, t) : T\mathcal{B}_0 \rightarrow T\mathcal{B}_t. \quad (2)$$

We will utilize the right Cauchy–Green deformation tensor and its inverse

$$\mathbf{C} = \mathbf{F}^t \cdot \mathbf{F} \quad \text{and} \quad \mathbf{C}^{-1} = \mathbf{F}^{-1} \cdot \mathbf{F}^{-t} \quad (3)$$

to define relevant strain measures. In particular, we introduce the Jacobian J and the trace I_1 as characteristic isotropic invariants,

$$J = \det(\mathbf{F}) \quad I_1 = \mathbf{C} : \mathbf{I} \quad (4)$$

and I_{ff} , I_{ss} , and I_{fs} as characteristic anisotropic invariants,

$$I_{\text{ff}} = \mathbf{C} : [\mathbf{f}_0 \otimes \mathbf{f}_0] \quad I_{\text{ss}} = \mathbf{C} : [\mathbf{s}_0 \otimes \mathbf{s}_0] \quad I_{\text{fs}} = \mathbf{C} : [\mathbf{f}_0 \otimes \mathbf{s}_0]^{\text{sym}}, \quad (5)$$

where $[\circ]^{\text{sym}} = \frac{1}{2}[\circ] + \frac{1}{2}[\circ]^t$ extracts the symmetric part of a second-order tensor $[\circ]$. Here, I_{ff} and I_{ss} are the stretches squared along the myocardial fiber and sheet directions, which we denote by \mathbf{f}_0 and \mathbf{s}_0 in the reference configuration \mathcal{B}_0 and by $\mathbf{f} = \mathbf{F} \cdot \mathbf{f}_0$ and $\mathbf{s} = \mathbf{F} \cdot \mathbf{s}_0$ in the current configuration \mathcal{B}_t .

2.2. Balance equations

The balance equation of the electrical problem balances the rate of change of the transmembrane potential ϕ with the divergence of the electrical flux, $\text{Div } \mathbf{Q}$, and the electrical source, F^ϕ ,

$$\dot{\phi} = \text{Div } \mathbf{Q} + F^\phi. \quad (6)$$

The balance equation of the mechanical problem balances the rate of change of the linear momentum with the divergence of the momentum flux, $\text{Div } \mathbf{P}$, where \mathbf{P} is the first Piola Kirchhoff stress tensor, and the momentum source, F^φ ,

$$\mathbf{0} = \text{Div } \mathbf{P} + F^\varphi. \quad (7)$$

Here, the divergences $\text{Div } \mathbf{Q}$ and $\text{Div } \mathbf{P}$ of the electrical and mechanical fluxes refer to the undeformed reference configuration. For the sake of simplicity, we model the electrical problem (6) using the classical monodomain equation and model the mechanical problem (7) as quasi-static, such that the rate of change of the linear momentum vanishes identically. The balance of angular momentum is identically satisfied through the symmetry of the Cauchy stress $\boldsymbol{\sigma} = 1/J \mathbf{P} \cdot \mathbf{F}^t = \boldsymbol{\sigma}^t$.

2.3. Constitutive equations

The electrical and mechanical problems (6) and (7) are coupled constitutively through the corresponding flux and source terms. The electrical flux \mathbf{Q} is typically introduced phenomenologically and characterizes the propagation speed of the electrical signal. It is usually proportional to the potential gradient $\nabla\phi$ and can potentially be coupled to the mechanical problem through the deformation gradient $\nabla\boldsymbol{\varphi}$ to account for stretch-induced changes in the propagation speed,

$$\mathbf{Q} = \mathbf{Q}(\nabla\phi, \nabla\boldsymbol{\varphi}). \quad (8)$$

The electrical source F^ϕ characterizes the electrophysiology of the individual cells on the local level. Through voltage-gated ion channels, F^ϕ depends on the electrical potential ϕ . Through possible stretch-activated ion channels, F^ϕ may depend on the deformation gradient $\nabla\boldsymbol{\varphi}$. Through the cell's biochemistry, F^ϕ also depends on the set of internal variables collectively summarized in the vector \mathbf{q} , which, in our case, contains a set of gating variables g_{gate} and a set of ion concentrations c_{ion} [40],

$$F^\phi = F^\phi(\phi, \nabla\boldsymbol{\varphi}, \mathbf{q}). \quad (9)$$

The momentum flux \mathbf{P} is simply the Piola stress, which we can additively decompose into a passive and an active part according to Hill's classical muscle model [41]. The passive stress \mathbf{P}^{pas} depends on the deformation gradient $\nabla\boldsymbol{\varphi}$ and characterizes the passive myocardium. The active stress \mathbf{P}^{act} either depends on the electrical potential ϕ [42] or on the set of internal variables \mathbf{q} [34], as proposed here, and introduces coupling to the electrochemical problem. The two-field nature of the Piola stress introduces an additional dependance on the deformation gradient $\nabla\boldsymbol{\varphi}$,

$$\mathbf{P} = \mathbf{P}^{\text{pas}}(\nabla\boldsymbol{\varphi}) + \mathbf{P}^{\text{act}}(\nabla\boldsymbol{\varphi}, \mathbf{q}). \quad (10)$$

The momentum source F^φ characterizes volume forces such as gravity, which we assume to be negligibly small in the subsequent analyses,

$$F^\varphi = \mathbf{0}. \quad (11)$$

We will now illustrate the computational solution of the coupled chemo-electro-mechanical problem using a weighted residual-based finite element approach.

3. DISCRETE PROBLEM OF CHEMO-ELECTRO-MECHANICS

To discretize the continuous chemo-electro-mechanical problem, we rephrase the electrical and mechanical balance equations (6) and (7) in their residual formats,

$$\begin{aligned} \mathbf{R}^\phi &= \dot{\phi} - \text{Div } \mathbf{Q} - F^\phi \doteq 0 & \text{in } \mathcal{B}_0 \\ \mathbf{R}^\varphi &= -\text{Div } \mathbf{P} - \mathbf{F}^\varphi \doteq \mathbf{0} & \text{in } \mathcal{B}_0, \end{aligned} \quad (12)$$

where both are valid in the entire domain \mathcal{B}_0 . We then partition the boundary $\partial\mathcal{B}_0$ into disjoint parts $\partial\mathcal{B}_0^\phi$ and $\partial\mathcal{B}_0^\varphi$ for the electrical problem and equivalently into $\partial\mathcal{B}_0^Q$ and $\partial\mathcal{B}_0^P$ for the mechanical problem and prescribe the corresponding Dirichlet and Neumann boundary conditions,

$$\begin{aligned} \phi &= \bar{\phi} \text{ on } \partial\mathcal{B}_0^\phi & \mathbf{Q} \cdot \mathbf{N} &= \bar{T}^Q \text{ on } \partial\mathcal{B}_0^Q \\ \varphi &= \bar{\varphi} \text{ on } \partial\mathcal{B}_0^\varphi & \mathbf{P} \cdot \mathbf{N} &= \bar{T}^P \text{ on } \partial\mathcal{B}_0^P, \end{aligned} \quad (13)$$

where \mathbf{N} denotes the outward normal to $\partial\mathcal{B}_0$. To derive the weak forms of the electrical and mechanical problems \mathbf{G}^ϕ and \mathbf{G}^φ , we integrate the residual statements (12) over the domain \mathcal{B}_0 , multiply both with the scalar-valued and vector-valued test functions $\delta\phi$ in $H_1^0(\mathcal{B}_0)$ and $\delta\varphi$ in $H_1^0(\mathcal{B}_0)$, integrate them by parts, and apply the corresponding Neumann boundary conditions (13.2) and (13.4),

$$\begin{aligned} \mathbf{G}^\phi &= \int_{\mathcal{B}_0} \delta\phi \dot{\phi} dV + \int_{\mathcal{B}_0} \nabla\delta\phi \cdot \mathbf{Q} dV - \int_{\partial\mathcal{B}_0^Q} \delta\phi \bar{T}^Q dA - \int_{\mathcal{B}_0} \delta\phi F^\phi dV = 0 \quad \forall \delta\phi \\ \mathbf{G}^\varphi &= \int_{\mathcal{B}_0} \nabla\delta\varphi : \mathbf{P} dV - \int_{\partial\mathcal{B}_0^P} \delta\varphi \cdot \bar{T}^P dA - \int_{\mathcal{B}_0} \delta\varphi \cdot \mathbf{F}^\varphi dV = 0 \quad \forall \delta\varphi. \end{aligned} \quad (14)$$

3.1. Temporal discretization

For the temporal discretization, we partition the time interval of interest \mathcal{T} into n_{step} subintervals $[t_n, t]$ as $\mathcal{T} = \bigcup_{n=0}^{n_{\text{step}}-1} [t_n, t]$ and focus on a typical time slab $[t_n, t]$. Here and from now on, we omit the index $n+1$ associated with the current time step. We assume that the primary unknowns ϕ_n and φ_n and all derivable flux terms, source terms, and state variables are known at the beginning of the current interval. To approximate the material time derivative of the transmembrane potential ϕ , we apply a first-order finite difference scheme,

$$\dot{\phi} = [\phi - \phi_n] / \Delta t, \quad (15)$$

where $\Delta t := t - t_n > 0$ denotes the current time increment. To solve for the unknowns ϕ and φ , we then apply a classical backward Euler time integration scheme and evaluate the discrete set of governing equations (14) at the current time point t .

3.2. Spatial discretization

For the spatial discretization, we apply a C^0 -continuous interpolation of the transmembrane potential ϕ and of the deformation φ and introduce both ϕ and φ as global degrees of freedom at the node point level. We partition the domain of interest \mathcal{B}_0 into n_{el} elements \mathcal{B}_0^e as $\mathcal{B}_0 = \bigcup_{e=1}^{n_{\text{el}}} \mathcal{B}_0^e$. Using the isoparametric concept, we interpolate the trial functions $\phi^h, \varphi^h \in H_1(\mathcal{B}_0)$ on the element level with the same basis function N^ϕ and N^φ as the element geometry. Using the Bubnov–Galerkin approach, we interpolate the test functions $\delta\phi^h, \delta\varphi^h \in H_1^0(\mathcal{B}_0)$ on the element level with the same basis function N^ϕ and N^φ as the trial functions,

$$\begin{aligned} \delta\phi^h|_{\mathcal{B}_0^e} &= \sum_{i=1}^{n_{e\phi}} N_i^\phi \delta\phi_i & \phi^h|_{\mathcal{B}_0^e} &= \sum_{k=1}^{n_{e\phi}} N_k^\phi \phi_k \\ \delta\varphi^h|_{\mathcal{B}_0^e} &= \sum_{j=1}^{n_{e\varphi}} N_j^\varphi \delta\varphi_j & \varphi^h|_{\mathcal{B}_0^e} &= \sum_{l=1}^{n_{e\varphi}} N_l^\varphi \varphi_l. \end{aligned} \quad (16)$$

We then rephrase the residuals of the electrical and mechanical problems (12) in their discrete forms,

$$\begin{aligned} \mathbf{R}_I^\phi &= \mathbf{A} \int_{\mathcal{B}_0^e} N_i^\phi \frac{1}{\Delta t} [\phi - \phi_n] + \nabla N_i^\phi \cdot \mathbf{Q} - N_i^\phi F^\phi dV_e - \int_{\partial \mathcal{B}_0^e} N_i^\phi \bar{T}^Q dA_e = 0 \\ \mathbf{R}_J^\varphi &= \mathbf{A} \int_{\mathcal{B}_0^e} \nabla N_j^\varphi \cdot \mathbf{P} - N_j^\varphi F^\varphi dV_e - \int_{\partial \mathcal{B}_0^e} N_j^\varphi \bar{T}^P dA_e = \mathbf{0}. \end{aligned} \tag{17}$$

Here, the operator \mathbf{A} symbolizes the assembly of all element contributions at the local electrical and mechanical element nodes $i = 1, \dots, n_{e\phi}$ and $j = 1, \dots, n_{e\varphi}$ to the overall residuals at the global electrical and mechanical nodes $I = 1, \dots, n_{n\phi}$ and $J = 1, \dots, n_{n\varphi}$.

3.3. Linearization

To solve the resulting coupled nonlinear system of equations (17), we propose a monolithic incremental iterative Newton–Raphson solution strategy based on consistent linearization of the governing equations [36]

$$\begin{aligned} \mathbf{R}_{I^{k+1}}^\phi &= \mathbf{R}_{I^k}^\phi + \sum_K \mathbf{K}_{IK}^{\phi\phi} d\phi_K + \sum_L \mathbf{K}_{IL}^{\phi\varphi} \cdot d\varphi_L \doteq 0 \\ \mathbf{R}_{J^{k+1}}^\varphi &= \mathbf{R}_{J^k}^\varphi + \sum_K \mathbf{K}_{JK}^{\varphi\phi} d\phi_K + \sum_L \mathbf{K}_{JL}^{\varphi\varphi} \cdot d\varphi_L \doteq 0 \end{aligned} \tag{18}$$

in terms of the following iteration matrices,

$$\begin{aligned} \mathbf{K}_{IK}^{\phi\phi} &= \frac{d\mathbf{R}_I^\phi}{d\phi_K} = \mathbf{A} \int_{\mathcal{B}_0^e} N_i^\phi \frac{1}{\Delta t} N_k^\phi - N_i^\phi d_\phi F^\phi N_k^\phi dV_e \\ &\quad + \mathbf{A} \int_{\mathcal{B}_0^e} \nabla N_i^\phi \cdot d_{\nabla\phi} \mathbf{Q} \cdot \nabla N_k^\phi dV_e \\ \mathbf{K}_{IL}^{\phi\varphi} &= \frac{d\mathbf{R}_I^\phi}{d\varphi_L} = \mathbf{A} \int_{\mathcal{B}_0^e} N_i^\phi \cdot d_F F^\phi \nabla N_l^\varphi dV_e \\ &\quad + \mathbf{A} \int_{\mathcal{B}_0^e} \nabla N_i^\phi \cdot d_F \mathbf{Q} \cdot \nabla N_l^\varphi dV_e \\ \mathbf{K}_{JK}^{\varphi\phi} &= \frac{d\mathbf{R}_J^\varphi}{d\phi_K} = \mathbf{A} \int_{\mathcal{B}_0^e} \nabla N_j^\varphi \cdot d_\phi \mathbf{P} N_k^\phi dV_e \\ \mathbf{K}_{JL}^{\varphi\varphi} &= \frac{d\mathbf{R}_J^\varphi}{d\varphi_L} = \mathbf{A} \int_{\mathcal{B}_0^e} \nabla N_j^\varphi \cdot d_F \mathbf{P} \nabla N_l^\varphi dV_e. \end{aligned} \tag{19}$$

The solution of the system of equations (18) renders the iterative update for the increments of the global unknowns $\phi_I \leftarrow \phi_I + d\phi_I$ and $\varphi_J \leftarrow \varphi_J + d\varphi_J$.

4. MODEL PROBLEM OF CHEMO-ELECTRO-MECHANICS

In this section, we briefly summarize the constitutive equations of the electrical flux, electrical source, and mechanical flux. In the discrete setting, we evaluate these equations on the integration point level, where we store the set of internal variables \mathbf{q} once the global Newton–Raphson iteration (18) has converged [42].

4.1. Electrical flux

The electrical flux \mathbf{Q} in equation (17.1) is typically assumed to depend on both the potential gradient $\nabla\phi$ and the deformation gradient $\nabla\varphi$. We now specify this dependency to be multiplicative. In

analogy to Fick’s law of diffusion and Fourier’s law of heat conduction, we apply Ohm’s law and assume that the electrical flux \mathbf{Q} is proportional to the gradient of the electrical potential $\nabla\phi$,

$$\mathbf{Q} = \mathbf{D} \cdot \nabla\phi \quad \text{with} \quad \mathbf{D} = d^{\text{iso}}\mathbf{C}^{-1} + d^{\text{ani}}\mathbf{f}_0 \otimes \mathbf{f}_0. \quad (20)$$

The second-order conductivity tensor \mathbf{D} can account for both isotropic propagation d^{iso} and anisotropic propagation d^{ani} along preferred directions \mathbf{f}_0 . Stretch-induced changes in the propagation speed are incorporated indirectly through the inverse left Cauchy–Green tensor $\mathbf{C}^{-1} = \mathbf{F}^{-1} \cdot \mathbf{F}^{-t}$ motivated by the assumption of a spatial rather than material isotropy [42], for which the isotropic term would simply scale with the second-order identity tensor \mathbf{I} . To evaluate the iteration matrices (19.1) and (19.2), we perform the consistent linearization of the electrical flux \mathbf{Q} with respect to the electrical gradient $d_{\nabla\phi}\mathbf{Q}$ and with respect to the deformation gradient $d_{\mathbf{F}}\mathbf{Q}$, where the former is nothing but the conductivity tensor \mathbf{D} and the latter reflect the aforementioned stretch-induced change in the propagation speed, see [42] for details.

4.2. Electrical source

The electrical source F^ϕ in equation (17.1) is a result of the local electrophysiology on the cellular level. As such, it is a function of the electrical potential ϕ , the deformation gradient $\nabla\phi$, and a set of internal variables \mathbf{q} , which characterize the electrochemical behavior of the cell. For the simplest possible models, \mathbf{q} only contains a single variable, the phenomenological recovery variable r [38, 43]. For the particular ventricular cardiomyocytes, we consider here [22, 23, 44], \mathbf{q} contains a total of 17 variables, that is, $n_{\text{gate}} = 13$ gating variables $g_{\text{gate}} = [g_m, g_h, g_j, g_{xr1}, g_{xr2}, g_{xs}, g_r, g_s, g_d, g_f, g_{xK1\infty}, g_{fCa}, g_g]$ and $n_{\text{ion}} = 4$ ion concentrations $c_{\text{ion}} = [c_{Na}, c_K, c_{Ca}, c_{Ca}^{\text{sr}}]$. These state variables define $n_{\text{crt}} = 15$ ionic currents $I_{\text{crt}} = [I_{Na}, I_{bNa}, I_{NaK}, I_{NaCa}, I_{K1}, I_{Kr}, I_{Ks}, I_{pK}, I_{t0}, I_{CaL}, I_{bCa}, I_{pCa}, I_{\text{leak}}, I_{\text{up}}, I_{\text{rel}}]$, as illustrated in Figure 2. The electrical source F^ϕ is directly related to the negative sum of all these currents I_{crt} across the cell membrane due to the outward positive convention established in experiments,

$$F^\phi = -[I_{Na} + I_{bNa} + I_{NaK} + I_{NaCa} + I_{K1} + I_{Kr} + I_{Ks} + I_{pK} + I_{t0} + I_{CaL} + I_{bCa} + I_{pCa}]. \quad (21)$$

Here, I_{Na} is the fast sodium current, I_{bNa} is the background sodium current, I_{NaK} is the sodium potassium pump current, I_{NaCa} is the sodium calcium exchanger current, I_{K1} is the inward rectifier current, I_{Kr} and I_{Ks} are the rapid and slow delayed rectifier currents, I_{pK} is the plateau potassium current, I_{CaL} is the long-lasting L-type calcium current, I_{bCa} is the background calcium current, and I_{pCa} is the plateau calcium current. In addition, we also have three intracellular currents, I_{leak} is the

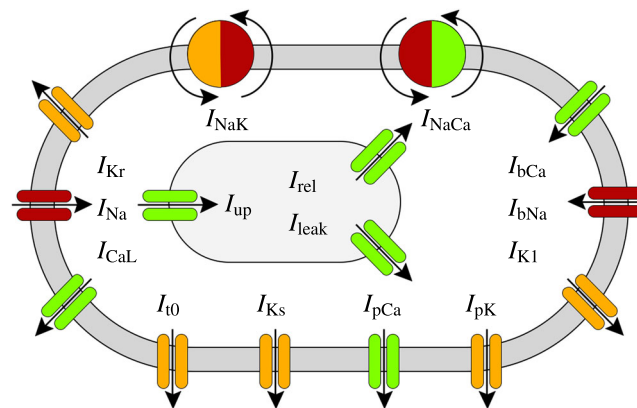


Figure 2. Human ventricular cardiomyocyte model with 15 ionic currents resulting from 10 transmembrane channels, one exchanger, and one pump. Three additional currents characterize ionic changes inside the sarcoplasmic reticulum, shown in grey. Sodium currents are indicated in red, potassium currents in orange, and calcium currents in green.

leakage current, I_{up} is the sarcoplasmic reticulum uptake current, and I_{rel} is the sarcoplasmic reticulum release current. For our particular cell model, none of the channels are mechanically gated, that is, all currents are independent of the deformation gradient $\nabla\boldsymbol{\varphi}$. Instead, all channels are voltage gated and their currents depend on the electrical potential ϕ . In addition, the currents depend on the set of internal variables \boldsymbol{q} consisting of the chemical state variables, that is, the gating variables g_{gate} and the ion concentrations c_{ion} . We can characterize all ionic currents through generic equations of the following generic form,

$$I_{\text{crt}} = I_{\text{crt}}(\phi, g_{\text{gate}}, c_{\text{ion}}), \quad (22)$$

which we specify in detail in the Appendix. From a mathematical point of view, the chemical problem is defined in terms of two sets of state variables, the n_{gate} gating variables g_{gate} and the n_{ion} ion concentrations c_{ion} . Both are governed through ordinary differential equations depending on the transmembrane potential ϕ , on the gating variables g_{gate} and on the ion concentrations c_{ion} ,

$$\begin{aligned} \dot{g}_{\text{gate}} &= f_{\text{gate}}(\phi, g_{\text{gate}}, c_{\text{ion}}) \\ \dot{c}_{\text{ion}} &= f_{\text{ion}}(\phi, g_{\text{gate}}, c_{\text{ion}}). \end{aligned} \quad (23)$$

The gating variables g_{gate} characterize the states of the individual ion channels, either open or close. They are defined through a set of ordinary differential equations of Hodgkin–Huxley type,

$$\dot{g}_{\text{gate}} = \left[g_{\text{gate}}^{\infty}(\phi, c_{\text{ion}}) - g_{\text{gate}} \right] / \tau_{\text{gate}}(\phi), \quad (24)$$

which we specify in detail in the Appendix. Here, g_{gate}^{∞} is a steady-state value and τ_{gate} is the time constant for reaching this steady state. Both are usually exponential functions of the membrane potential ϕ . The ion concentrations inside the cell c_{ion} change in response to the transmembrane currents I_{crt} . For our particular cardiomyocyte model, the relevant ion concentrations are the sodium c_{Na} , potassium c_{K} , and calcium concentrations c_{Ca} , and the calcium concentration in the sarcoplasmic reticulum $c_{\text{Ca}}^{\text{sr}}$. Collectively, these ion concentrations c_{ion} are defined through a set of ordinary differential equations,

$$\begin{aligned} \dot{c}_{\text{Na}} &= -\frac{C}{VF} [I_{\text{Na}} + I_{\text{bNa}} + 3I_{\text{NaK}} + 3I_{\text{NaCa}}] \\ \dot{c}_{\text{K}} &= -\frac{C}{VF} [I_{\text{K1}} + I_{\text{Kr}} + I_{\text{Ks}} - 2I_{\text{NaK}} + I_{\text{pK}} + I_{\text{t0}} + I_{\text{stim}}] \\ \dot{c}_{\text{Ca}} &= -\frac{C}{2VF} [I_{\text{CaL}} + I_{\text{bCa}} + I_{\text{pCa}} - 2I_{\text{NaCa}}] \gamma_{\text{Ca}} + [I_{\text{leak}} - I_{\text{up}} + I_{\text{rel}}] \gamma_{\text{Ca}} \\ \dot{c}_{\text{Ca}}^{\text{sr}} &= +\frac{V}{V^{\text{sr}}} [I_{\text{up}} - I_{\text{leak}} - I_{\text{rel}}] \gamma_{\text{Ca}}^{\text{sr}}. \end{aligned} \quad (25)$$

Here, C is the membrane capacitance per unit surface area, V is the cytoplasmic volume, V^{sr} is the volume of the sarcoplasmic reticulum, F is the Faraday constant, and γ_{Ca} and $\gamma_{\text{Ca}}^{\text{sr}}$ are the scaling coefficients. Although the electrical and mechanical problems are global in nature, the chemical problem remains strictly local. When using a finite element discretization, this allows us to store the chemical state variables g_{gate} and c_{ion} locally as internal variables on the integration point level. It is obvious that their complex, nonlinear coupled system of ordinary differential equations (24) and (25) cannot be solved analytically. Here, we apply a numerical solution using an implicit Euler backward time-stepping scheme embedded in a local Newton iteration. To evaluate the iteration matrices (19.1) and (19.2), we perform the consistent linearization of the electrical source F^{ϕ} with respect to the transmembrane potential $d_{\phi} F^{\phi}$ related to voltage-gated ion channels and with respect to the deformation gradient $d_{\boldsymbol{F}} F^{\phi}$ related to stretch-activated ion channels [40]. For our particular cell model, in the absence of stretch-activated ion channels, the second term vanishes identically.

4.3. Mechanical flux

The momentum flux \boldsymbol{P} in equation (17.2) depends on both the electrical potential ϕ and deformation gradient $\boldsymbol{\varphi}$. We adopt the common assumption to decompose the overall stress additively into

a passive mechanically induced part \mathbf{P}^{pas} and an active electrically induced part \mathbf{P}^{act} , such that $\mathbf{P} = \mathbf{P}^{\text{pas}} + \mathbf{P}^{\text{act}}$. For the passive Piola stress, we select a compressible orthotropic model [45, 46],

$$\begin{aligned} \mathbf{P}^{\text{pas}} = & \kappa [J - 1] \mathbf{F}^{-t} \\ & + a \exp(b [I_1 - 3]) \mathbf{F} \\ & + 2a_{\text{ff}} [I_{\text{ff}} - 1] \exp(b_{\text{ff}} [I_{\text{ff}} - 1]^2) \mathbf{f} \otimes \mathbf{f}_0 \\ & + 2a_{\text{ss}} [I_{\text{ss}} - 1] \exp(b_{\text{ss}} [I_{\text{ss}} - 1]^2) \mathbf{s} \otimes \mathbf{s}_0 \\ & + a_{\text{fs}} I_{\text{fs}} \exp(b_{\text{fs}} I_{\text{fs}}^2) \mathbf{f} \otimes \mathbf{s}_0 \\ & + a_{\text{fs}} I_{\text{fs}} \exp(b_{\text{fs}} I_{\text{fs}}^2) \mathbf{s} \otimes \mathbf{f}_0, \end{aligned} \quad (26)$$

parameterized in terms of the isotropic invariants J and I_1 and the anisotropic invariants I_{ff} , I_{ss} , and I_{fs} , weighted by the bulk modulus κ and the four sets of parameters a and b [47, 48]. Here, rather than using the original quasi-incompressible formulation proposed in the literature [46], for conceptual simplicity, we assume that the myocardial tissue is decently compressible because of its vascular network [49]. More recent cardiac models additionally even account for tissue porosity and models the myocardium as porous medium [50], an approach that we do not pursue here. For the active Piola stress \mathbf{P}^{act} , we assume that an increase in the intracellular calcium concentration c_{Ca} above a critical level $c_{\text{Ca}}^{\text{crit}}$ induces an active cardiomyocyte contraction F^{act} [51, 52], which is acting along the fiber direction \mathbf{f}_0 [42, 53]. The contractile force F^{act} displays a twitch-type behavior [54], with a smooth off-on transition characterized through the twitch-function ϵ

$$\begin{aligned} \mathbf{P}^{\text{act}} &= F^{\text{act}} \mathbf{f} \otimes \mathbf{f}_0 \\ \dot{F}^{\text{act}} &= \epsilon [\eta [c_{\text{Ca}} - c_{\text{Ca}}^{\text{rest}}] - F^{\text{act}}] \\ \epsilon &= \epsilon_0 + [\epsilon_\infty - \epsilon_0] \exp(-\exp(-\xi [c_{\text{Ca}} - c_{\text{Ca}}^{\text{crit}}])). \end{aligned} \quad (27)$$

Here, η controls the saturation of the active contractile force F^{act} , $c_{\text{Ca}}^{\text{rest}}$ is the resting concentration, ϵ_0 and ϵ_∞ are the minimum and maximum values of ϵ , $c_{\text{Ca}}^{\text{crit}}$ is the limit value above which contraction is initiated, and ξ is the transition rate from ϵ_0 to ϵ_∞ at $c_{\text{Ca}}^{\text{crit}}$ [42]. More sophisticated constitutive models for active stress generation additionally include a velocity dependence [35, 55] and fully three-dimensional effects [10]. Alternatively, recent approaches suggest to model active contraction kinematically through the multiplicative decomposition of the deformation gradient [56, 57]. To evaluate the iteration matrices (19.3) and (19.4), we perform the consistent linearization of the Piola stress \mathbf{P} with respect to the transmembrane potential $d_\phi \mathbf{P}$ related to the active stress and with respect to the deformation gradient $d_{\mathbf{F}} \mathbf{P}$ related mainly to the passive stress [45].

5. EXAMPLES

5.1. Chemo-electro-mechanical coupling in a single cell

To illustrate the local features of our chemo-electrical-mechanical model, we simulate the electrophysiology of an epicardial human ventricular cardiomyocyte throughout a representative excitation cycle. For the chemical parameters, we use the values summarized in Table I. For the electromechanical coupling parameters, we choose the saturation of cardiomyocyte contraction to $\eta = 12.5 \text{ kPa}/\mu\text{M}$, the resting concentration of calcium to $c_{\text{Ca}}^{\text{rest}} = 0.05 \mu\text{M}$, the minimum and maximum values scaling fiber contraction to $\epsilon_0 = 0.1/\text{ms}$ and $\epsilon_\infty = 1.0 \text{ ms}$, the critical calcium concentration previously mentioned, which contraction is initiated to $c_{\text{Ca}}^{\text{crit}} = 0.8 \mu\text{M}$, and the transition rate to $\xi = 4.0/\mu\text{M}$. We initialize the global membrane potential with $\phi = -86 \text{ mV}$ and the local ion concentrations with $c_{\text{Na}} = 11.6 \text{ mM}$, $c_{\text{K}} = 138.3 \text{ mM}$, and $c_{\text{Ca}} = 0.08 \mu\text{M}$, mimicking the resting state. For the gating variables, we choose the following initial conditions $g_{\text{m}} = 0$, $g_{\text{h}} = 0.75$, $g_{\text{j}} = 0.75$, $g_{\text{d}} = 0$, $g_{\text{f}} = 1$, $g_{\text{fCa}} = 1$, $g_{\text{r}} = 0$, $g_{\text{s}} = 1$, $g_{\text{xs}} = 0$, $g_{\text{xr1}} = 0$, $g_{\text{xr2}} = 0$, $g_{\text{xK1}\infty} = 0.05$, and $g_{\text{g}} = 1$. To initiate a characteristic action potential, we apply an initial electrical stimulus slightly above the critical stimulation threshold [40].

Table I. Chemo-electrical material parameters of human ventricular cardiomyocyte.

	Sodium related	Potassium related	Calcium related	Calcium ^{sr} related
Concentrations	$c_{Na0} = 140 \text{ mM}$	$c_{K0} = 5.4 \text{ mM}$	$c_{Ca0} = 2 \text{ mM}$	-
Maximum currents	$I_{NaCa}^{\max} = 1000 \text{ pA/pF}$ $I_{NaK}^{\max} = 1.362 \text{ pA/pF}$	$I_{NaK}^{\max} = 1.362 \text{ pA/pF}$	$I_{NaCa}^{\max} = 1000 \text{ pA/pF}$ $I_{NaCa}^{\max} = 0.08 \text{ s}^{-1}$ $I_{leak}^{\max} = 0.425 \text{ mM/s}$ $I_{up}^{\max} = 8.232 \text{ mM/s}$ $I_{rel}^{\max} = 8.232 \text{ mM/s}$	$I_{leak}^{\max} = 0.08 \text{ s}^{-1}$ $I_{rel}^{\max} = 0.425 \text{ mM/s}$ $I_{up}^{\max} = 8.232 \text{ mM/s}$
Maximum conductances	$C_{Na}^{\max} = 14.838 \text{ nS/pF}$ $C_{bNa}^{\max} = 0.00029 \text{ nS/pF}$	$C_{Kl}^{\max} = 5.405 \text{ nS/pF}$ $C_{Kr}^{\max} = 0.0096 \text{ nS/pF}$ $C_{Ks}^{\max} = 0.245 \text{ nS/pF}$ $C_{Ks, epi}^{\max} = 0.245 \text{ nS/pF}$ $C_{Ks, endo}^{\max} = 0.245 \text{ nS/pF}$ $C_{Ks, M}^{\max} = 0.062 \text{ nS/pF}$ $C_{pk}^{\max} = 0.0146 \text{ nS/pF}$ $C_{10}^{\max} = 0.294 \text{ nS/pF}$ $C_{10, epi}^{\max} = 0.294 \text{ nS/pF}$ $C_{10, endo}^{\max} = 0.073 \text{ nS/pF}$ $C_{10, M}^{\max} = 0.294 \text{ nS/pF}$	$C_{Ca}^{\max} = 0.175 \text{ mm}^3 / [\mu\text{Fs}]$ $C_{CaL}^{\max} = 0.000592 \text{ nS/pF}$ $C_{bCa}^{\max} = 0.825 \text{ pA/pF}$ C_{pCa}^{\max}	
Half saturation constants	$c_{CaNa} = 1.38 \text{ mM}$ $c_{NaCa} = 87.50 \text{ mM}$ $c_{KNa} = 1.00 \text{ mM}$ $c_{NaK} = 40.00 \text{ mM}$	$c_{KNa} = 1.00 \text{ mM}$ $c_{NaK} = 40.00 \text{ mM}$	$c_{CaNa} = 1.38 \text{ mM}$ $c_{NaCa} = 87.50 \text{ mM}$ $c_{pCa} = 0.0005 \text{ mM}$ $c_{up} = 0.00025 \text{ mM}$ $c_{rel} = 0.25 \text{ mM}$ $c_{buf} = 0.001 \text{ mM}$	$c_{up} = 0.00025 \text{ mM}$ $c_{rel} = 0.25 \text{ mM}$ $c_{buf}^{\text{sr}} = 0.3 \text{ mM}$
Other parameters	$k_{NaCa}^{\text{sat}} = 0.10$ $\gamma_{NaCa} = 2.50$ $\gamma = 0.35$	$\rho_{KNa} = 0.03$	$\gamma_{rel} = 2$ $c_{tot} = 0.15 \text{ mM}$	$\gamma_{rel} = 2$ $c_{tot}^{\text{sr}} = 10 \text{ mM}$
Gas constant Faraday constant	$R = 8.3143 \text{ J K}^{-1} \text{ mol}^{-1}$ $F = 96.4867 \text{ C/mmol}$	Temperature $T = 310 \text{ K}$ Membrane capacitance $C = 185 \text{ pF}$	Cytoplasmic volume Sarcoplasmic reticulum volume	$V = 16,404 \mu\text{m}^3$ $V^{\text{sr}} = 1094 \mu\text{m}^3$

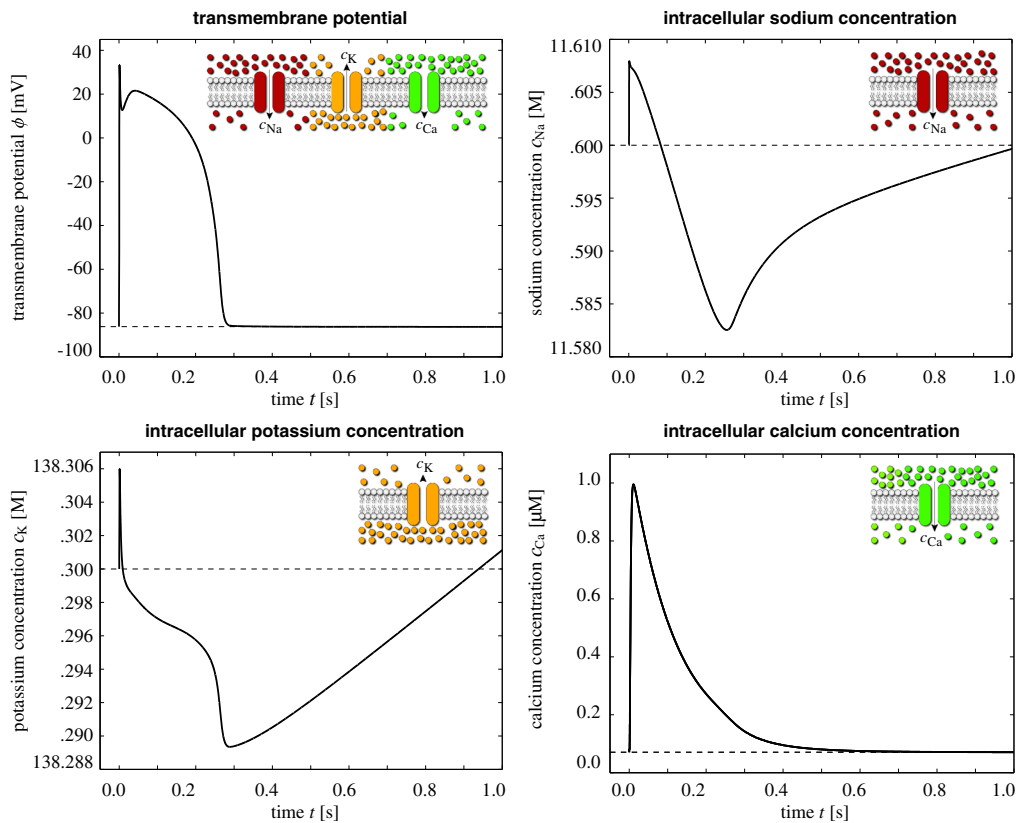


Figure 3. Electrochemistry in a human ventricular cardiomyocyte. Temporal evolution of the transmembrane potential ϕ and of the intracellular sodium potassium and calcium concentrations c_{Ca} , c_K , and c_{Ca} . The influx of positively charged sodium ions generates a rapid upstroke in the transmembrane potential. At peak, the efflux of positively charged potassium ions initiates an early, partial repolarization. During the plateau, the influx of positively charged calcium ions balances the efflux of positively charged potassium ions. Final repolarization begins when the efflux of potassium ions exceeds the influx of calcium ions. Throughout the interval between the end of repolarization and beginning of the next cycle, the cell is at rest.

Figure 3, top left, illustrates the evolution of the transmembrane potential ϕ . In cardiac cells at rest, the transmembrane potential is -86 mV, which implies that the intracellular domain is negatively charged in comparison with the extracellular domain. The application of an external stimulus generates an initial depolarization across the cell membrane. Once the stimulus exceeds the critical threshold, the transmembrane potential increases rapidly from its resting state of -86 mV via an overshoot of $+38$ mV to its excited state of $+20$ mV. After a brief period of partial initial repolarization, the transmembrane potential experiences a characteristic plateau of 0.2 ms, before the cell gradually repolarizes to return to its initial resting state.

Figure 3, top right, illustrates the evolution of the intracellular sodium concentration c_{Na} , which rises sharply at the beginning of the cycle to create the rapid upstroke of the transmembrane potential. The sodium concentration then decays slowly toward the end of the repolarization phase and increases gradually during the resting phase to return to its initial value. Figure 3, bottom left, illustrates the evolution of the intracellular potassium concentration c_K . After a rapid increase, c_K decreases in a stepwise fashion, regulated by the sequential activation of the individual potassium channels. At the end of the repolarization phase, c_K increases gradually to smoothly return to its initial value. Figure 3, bottom right, illustrates the evolution of the intracellular calcium concentration c_{Ca} . Slightly after the upstroke of the transmembrane potential, the calcium concentration increases to its peak value and then decays smoothly to its original value throughout the remaining phases of the cycle. In the following section, we will demonstrate how an increase in the intracellular calcium

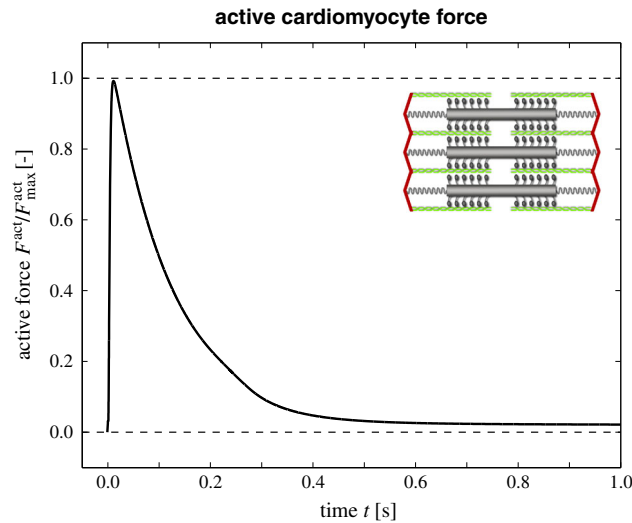


Figure 4. Mechanical contraction in a human ventricular cardiomyocyte. Temporal evolution of the active force F^{act} throughout an excitation cycle. The rapid increase in the intracellular calcium concentration c_{Ca} initiates a rapid increase in the active force. After reaching its peak value, the force gradually returns to 0.

concentration can initiate mechanical contraction. In summary, the model reproduces all characteristic features of human ventricular cardiomyocytes [23, 40, 58]: an initial increase in sodium to create a rapid upstroke in the transmembrane potential, a combined decrease in potassium and increase in calcium to generate the characteristic plateau, and an increase in potassium during the recovery phase to bring the cell back to its resting state. Despite drastic changes in the membrane potential from -86 mV to $+20$ mV, changes in the individual ion concentrations remain remarkably small, typically in the order of less than 1%.

Figure 4 illustrates the evolution of the active contractile force F^{act} throughout an excitation cycle. The rapid increase in the intracellular calcium concentration c_{Ca} initiates a rapid increase in the active force. After reaching its peak value, the force gradually returns to 0.

5.2. Chemo-electro-mechanical coupling in a square panel

To demonstrate the convergence of our chemo-electrical-mechanical model, we simulate the wave propagation in a square flat panel and compare the activation times for different spatial and temporal discretizations. In particular, we discretize the 8×8 mm panel with epicardial human ventricular cardiomyocytes using the material parameters summarized in Tables I and II. We initialize the panel with homogeneous initial conditions for the local ion concentrations and local gating variables using the same parameter values as described in Section 5.1 to mimic the initial resting state. We initialize the global membrane potential with a resting value of $\phi = -86$ mV and perturb its value at the upper edge of the panel with a value of $\phi = +40$ mV to initiate a downward traveling wave.

For the spatial convergence study, we discretize the panel in space with $n \times n \times 12$ linear tetrahedral elements, $(n + 1) \times (n + 1) \times 3$ nodes and $(n + 1) \times (n + 1) \times 12$ degrees of freedom, where we systematically increase n from 8 to 44 in steps of four. Accordingly, our finest mesh thus consists of 23,232 elements, 6,075 nodes, and 24,300 degrees of freedom. For this study, we fix the temporal discretization at a constant time step size of $\Delta t = 0.125$ ms. For the temporal convergence study, we discretize the travel time with 40 to 975 equidistant finite difference steps and fix the spatial discretization at a constant mesh size parameterized with $n = 12$.

Figure 5, top, illustrates five representative spatial discretizations parameterized with $n = 12, 20, 28, 36,$ and 44 . Red colors indicate tissue regions that are already excited, and grey regions indicate tissue still at the resting state. All five snapshots correspond to $t = 2.00$ ms, the time at which the wave front has reached the centerline of the panel for the finest discretization, shown on the

Table II. Electromechanical material parameters of human cardiac tissue.

Electrical parameters		
Isotropic conduction septum	$d^{iso} = 5 \text{ mm}^2/\text{ms}$	[42]
Anisotropic conduction septum	$d^{ani} = 10 \text{ mm}^2/\text{ms}$	[42]
Isotropic conduction	$d^{iso} = 0.1 \text{ mm}^2/\text{ms}$	[42]
Anisotropic conduction	$d^{ani} = 0.2 \text{ mm}^2/\text{ms}$	[42]
Mechanical parameters		
Isotropic bulk	$\kappa = 100 \text{ kPa}$	
Isotropic myocardium	$a = 0.496 \text{ kPa}, b = 7.209$	[45]
Anisotropic myocardium	$a_{ff} = 15.193 \text{ kPa}, b_{ff} = 20.417$	[45]
	$a_{ss} = 3.283 \text{ kPa}, b_{ss} = 11.176$	[45]
	$a_{fs} = 0.662 \text{ kPa}, b_{fs} = 9.466$	[45]
Electromechanical parameters		
Saturation of contraction	$\eta = 12.5 \text{ kPa}/\mu\text{M}$	[42]
Resting calcium concentration	$c_{Ca}^{rest} = 0.05 \mu\text{M}$	[40]
Critical calcium concentration	$c_{Ca}^{crit} = 0.8 \mu\text{M}$	
Minimum activation	$\epsilon_0 = 0.1/\text{ms}$	[42]
Maximum activation	$\epsilon_\infty = 1.0/\text{ms}$	[42]
Transition rate	$\xi = 4.00/\mu\text{M}$	[42]

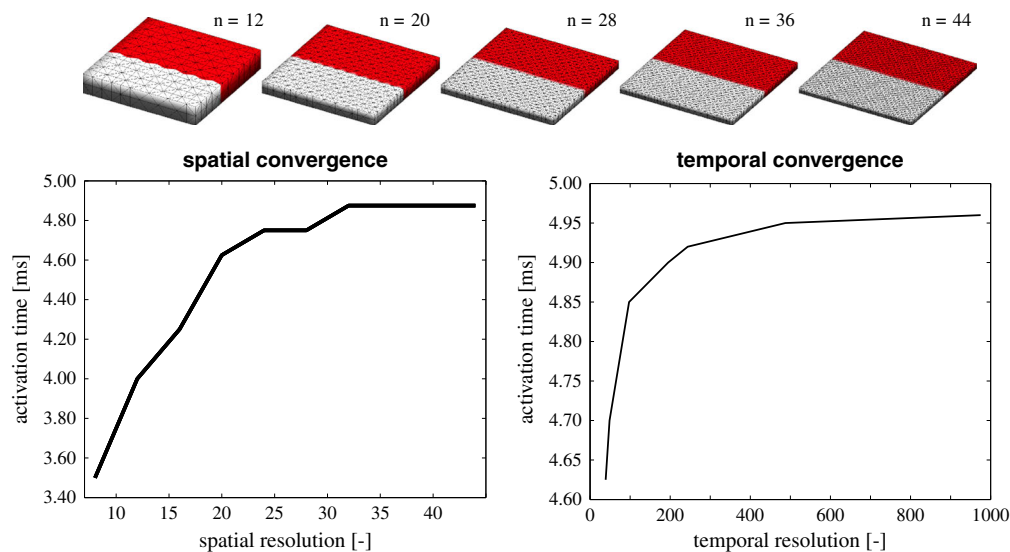


Figure 5. Algorithmic convergence upon spatial and temporal refinements. The panel is discretized in space with $n \times n \times 12$ tetrahedral elements, $(n+1) \times (n+1) \times 3$ nodes, and $(n+1) \times (n+1) \times 12$ degrees of freedom, where n is increased from 8 to 44. The activation sequence is discretized in time with 40 to 975 equidistant finite difference steps. Both spatial and temporal discretizations converge smoothly toward a finite activation time.

right. For the coarsest discretization, shown on the left, the wave has already passed the centerline, indicating that the wave speed is slightly higher for coarser meshes.

Figure 5, bottom, illustrates the algorithmic convergence upon spatial refinement, left, and temporal refinement, right. As a global metric for the traveling wave, we plot the activation time of the lower panel edge for different spatial and temporal discretizations. In agreement with the color-coded panels in the top row, both activation graphs reveal that the wave travels slightly faster for coarser spatial and temporal discretizations. However, upon spatial and temporal refinements, both solutions converge smoothly toward a finite activation time.

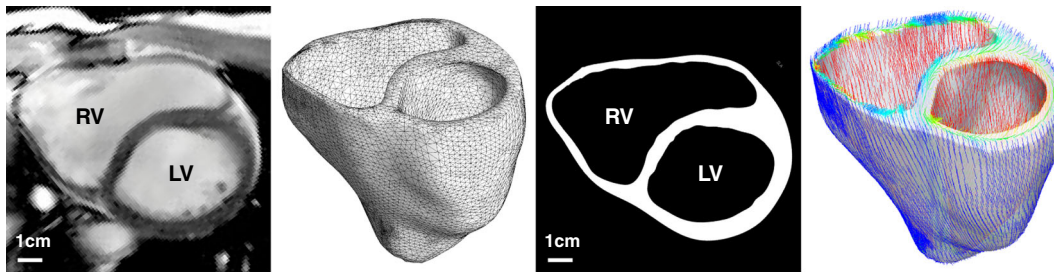


Figure 6. Human heart model created from magnetic resonance images, left. The mesh consists of 46,896 linear tetrahedral elements, 13,831 nodes, and 55,324 degrees of freedom, middle. The fiber orientation created from a feature-based Poisson interpolation varies gradually from -70° in the epicardium, the outer wall shown in blue, to $+80^\circ$ in the endocardium, the inner wall shown in red, right.

5.3. Chemo-electro-mechanical coupling in the human heart

To illustrate the global features of our chemo-electrical–mechanical model, we simulate excitation–contraction coupling in a human heart throughout a representative cardiac cycle. We reconstruct a patient-specific human heart model from magnetic resonance images [59], see Figure 6. Figure 6, middle, illustrates the finite element discretization consisting of 46,896 linear tetrahedral elements, 13,831 nodes, and 55,324 degrees of freedom. To account for the characteristic microstructure of the heart, we assign locally varying fiber vectors \mathbf{f}_0 and sheet vectors \mathbf{s}_0 created from a feature-based Poisson interpolation [60]. Specifically, we enforce the Poisson interpolation in the weak sense using a standard linear finite element algorithm for scalar-valued second-order boundary value problems. We introduce fiber and sheet angles as a global unknowns and enforce their epicardial and endocardial values in the strong sense as Dirichlet boundary conditions. We have previously demonstrated that this concept is capable of generating smoothly varying fibre orientations, quickly, efficiently, and robustly, both in a generic bi-ventricular model and in a patient-specific human heart [60]. Figure 6, right, illustrates the resulting fiber distribution across the left and right ventricles. Fiber directions vary gradually from -70° in the epicardium, the outer wall shown in blue, to $+80^\circ$ in the endocardium, the inner wall shown in red. Sheet directions are outward-pointing with respect to the epicardial surface.

Similar to the single cell example in Section 5.1, we apply initial conditions which mimic the resting state, with a global membrane potential of $\phi = -86$ mV and the local ion concentrations of $c_{\text{Na}} = 11.6$ mM, $c_{\text{K}} = 138.3$ mM, $c_{\text{Ca}} = 0.08$ μM , and $c_{\text{Ca}}^{\text{sr}} = 0.56$ mM and gating variables of $g_{\text{m}} = 0$, $g_{\text{h}} = 0.75$, $g_{\text{j}} = 0.75$, $g_{\text{d}} = 0$, $g_{\text{f}} = 1$, $g_{\text{fCa}} = 1$, $g_{\text{r}} = 0$, $g_{\text{s}} = 1$, $g_{\text{xs}} = 0$, $g_{\text{xr1}} = 0$, $g_{\text{xr2}} = 0$, $g_{\text{xK1}\infty} = 0.05$, and $g_{\text{g}} = 1$. Table I summarizes the chemo-electrical parameters which are similar to single cell example in Section 5.1. To account for regionally varying action potential durations, we divide the heart in five regions, basal septum, apical septum, apex, mid-ventricular wall, and lateral ventricular wall [61]. We systematically increase the bulk ion channel conductances $C_{\text{Kr}}^{\text{max}}$, $C_{\text{Ks}}^{\text{max}}$, and $C_{\text{CaL}}^{\text{max}}$ from upper septum to lateral wall by $\pm 30\%$. The electromechanical coupling parameters are the saturation of cardiomyocyte contraction $\eta = 12.5$ kPa/ μM , the resting concentration of calcium $c_{\text{Ca}}^{\text{rest}} = 0.05$ μM , the minimum and maximum values scaling fiber contraction $\epsilon_0 = 0.1/\text{ms}$ and $\epsilon_\infty = 1.0/\text{ms}$, the critical calcium concentration above which contraction is initiated $c_{\text{Ca}}^{\text{crit}} = 0.8$ μM , and the transition rate $\xi = 4.0/\mu\text{M}$. These are the same values as in the single cell example in Section 5.1, which have been calibrated such that the maximum fiber contraction λ_{ff} is approximately 15% [10]. The electrical parameters are the isotropic and anisotropic conduction $d^{\text{iso}} = 5$ mm²/ms and $d^{\text{ani}} = 10$ mm²/ms in the Purkinje fiber rich septal region and $d^{\text{iso}} = 0.1$ mm²/ms and $d^{\text{ani}} = 0.2$ mm²/ms in the lateral ventricular walls. We would like to point out though that the degree of anisotropy chosen here is relatively low as compared with physiological anisotropy ratios of 1:5 or even 1:10 [43]. Moreover, in reality, the Purkinje fibers are isolated from the septum and activate the heart from the endocardium of the left and right ventricular walls from the apex to about three-fourth of the total ventricular length. A discrete representation of the

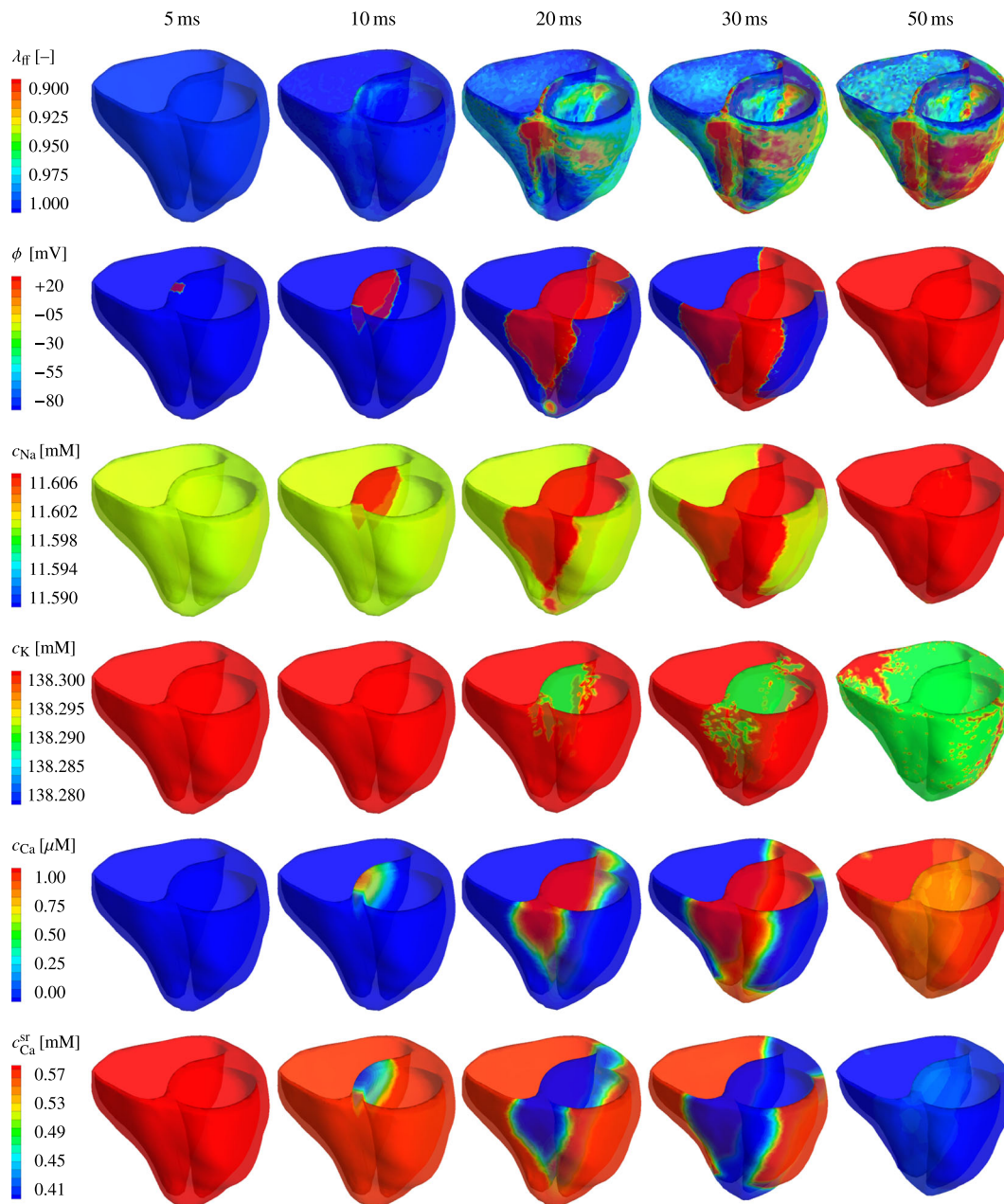


Figure 7. Chemo-electro-mechanical coupling in the human heart. Spatio-temporal evolution of the fiber contraction λ_{ff} , the transmembrane potential ϕ , the intracellular sodium, potassium, and calcium concentrations c_{Na} , c_K , and c_{Ca} and the calcium concentration in the sarcoplasmic reticulum c_{Ca}^{sr} during the rapid depolarization phase of the cardiac cycle. Changes in the individual ion concentrations initiate an increase in the transmembrane potential ϕ from -86 mV to $+20$ mV. Changes in the intracellular calcium concentration c_{Ca} initiate a mechanical contraction λ_{ff} of up to 10–15%. During the contraction phase, the apex moves rapidly toward the base, and the heart undergoes a clockwise rotation around its long axis.

Purkinje fiber network [59] would therefore provide a more accurate reflection of the excitation pattern with a more realistic representation of transmural activation gradients [10]. The mechanical parameters are the isotropic elastic bulk modulus $\kappa = 100.0$ kPa, isotropic elastic tissue parameters $a = 0.496$ kPa and $b = 7.209$, anisotropic elastic parameters, $a_{ff} = 15.193$ kPa and $b_{ff} = 20.417$,

$a_{ss} = 3.283$ kPa and $b_{ss} = 11.176$, and $a_{fs} = 0.662$ kPa and $b_{fs} = 9.466$, which we have identified [45] using simple shear experiments from the literature [46, 62]. Table II summarizes the electromechanical parameters.

For the electrical problem, we apply the common assumption of homogeneous Neumann boundary conditions. For the mechanical problem, we apply homogeneous Dirichlet boundary conditions throughout the basal plane [63]. We excite the heart through an external stimulus in the region of the atrioventricular node located in the center of the basal septum. We apply an adaptive time-stepping scheme, for which we select the convergence tolerance to $1.0E-09$ and the optimal number of iterations to four [40]. For a larger number of iterations, the adaptive scheme automatically decreases the time step size; for a smaller number of iterations, the adaptive scheme increases the time step size [37].

Figures 7 and 8 illustrate the evolution of the fiber contraction λ_{ff} , of the transmembrane potential ϕ , and of the individual ion concentrations c_{Na} , c_K , c_{Ca} , and c_{Ca}^{sr} during the depolarization and repolarization phases, respectively. Figure 7 shows how depolarization is initiated through changes in the intracellular sodium concentration c_{Na} , which increases rapidly within the first milliseconds of the cardiac cycle, third row. This increase is associated with a rapid increase in the membrane potential ϕ , second row, which, in turn, affects the voltage-gated calcium and potassium channels within the cell membrane. The intracellular calcium concentration c_{Ca} increases, fifth row. The intracellular potassium concentration c_K follows with a slight time delay of 15 ms, fourth row. The intracellular calcium concentration c_{Ca} increases further as calcium is released from the sarcoplasmic reticulum c_{Ca}^{sr} , sixth row. The increase in the intracellular calcium concentration directly initiates cardiomyocyte contraction λ_{ff} , first row. The contraction varies regionally and transmurally with maximum values of 10% and more, corresponding to $\lambda_{ff} = 0.90$ and less. As the heart contracts, the apex moves markedly upward toward the fixed base, columns four and five. After 50 ms, the heart is entirely depolarized. The transmembrane potential ϕ has reached its peak value of 20 mV throughout both ventricles, and the heart is maximally contracted.

Figure 8 displays the repolarization phase characterized through a smooth decrease of the transmembrane potential ϕ and the mechanical contraction λ_{ff} back to their resting values, first and second rows. Decrease in mechanical contraction is caused by a gradual decrease of the intracellular calcium c_{Ca} concentration back to its resting value, fifth row. The sarcoplasmic reticulum takes up the intracellular calcium, and c_{Ca}^{sr} returns back to its resting value, sixth row. At the same time, the intracellular sodium concentration c_{Na} , which has initially increased, now dips even below its initial value and reaches a minimum after 260 ms, third row. The intracellular potassium concentration c_K reaches its minimum approximately at the same time, fourth row. In the course of time, both sodium and potassium then slowly return to their resting values as their concentrations increase gradually. The temporal evolution of the mechanical, electrical, and chemical fields is in excellent qualitative and quantitative agreement with the single cardiomyocyte transients documented in Figures 3 and 4. However, because of the heterogeneous character of the whole heart simulation, the intracellular sodium and potassium concentrations c_{Na} and c_K still display small local deviations from the complete resting state 1000 ms after the onset of excitation, see Figure 8, third and fourth rows, last column.

Figure 9 illustrates the global performance of the heart in dry pumping in terms of two characteristic clinical metrics of cardiac function, apical lift δ and of ventricular torsion ϑ . Figure 9, left, shows the apical lift, that is, the vertical movement of the apex along the heart's long axis toward the fixed base. Shortly after the onset of excitation, the apex lifts rapidly toward the base moving upward by approximately 8 mm. Figure 9, right, shows the ventricular torsion, that is, the rotation of two marked locations in the lateral left ventricular wall, at approximately 1/3 and 2/3 height, around the heart's long axis. Shortly after the onset of excitation, the heart undergoes a rapid twist, rotating clockwise by approximately 6° and 13° , with the amount of torsion increasing from the fixed base to the free apex. Both apical lift and ventricular torsion then decrease gradually to 0 as the heart returns to its original position. These characteristics of apical lift and ventricular torsion are in excellent qualitative agreement with clinical observations [64].

Figure 10 demonstrates the performance of our fully implicit monolithic finite-element based algorithm. Figure 10, left, shows the variation of the time step size and Figure 10, right, shows the

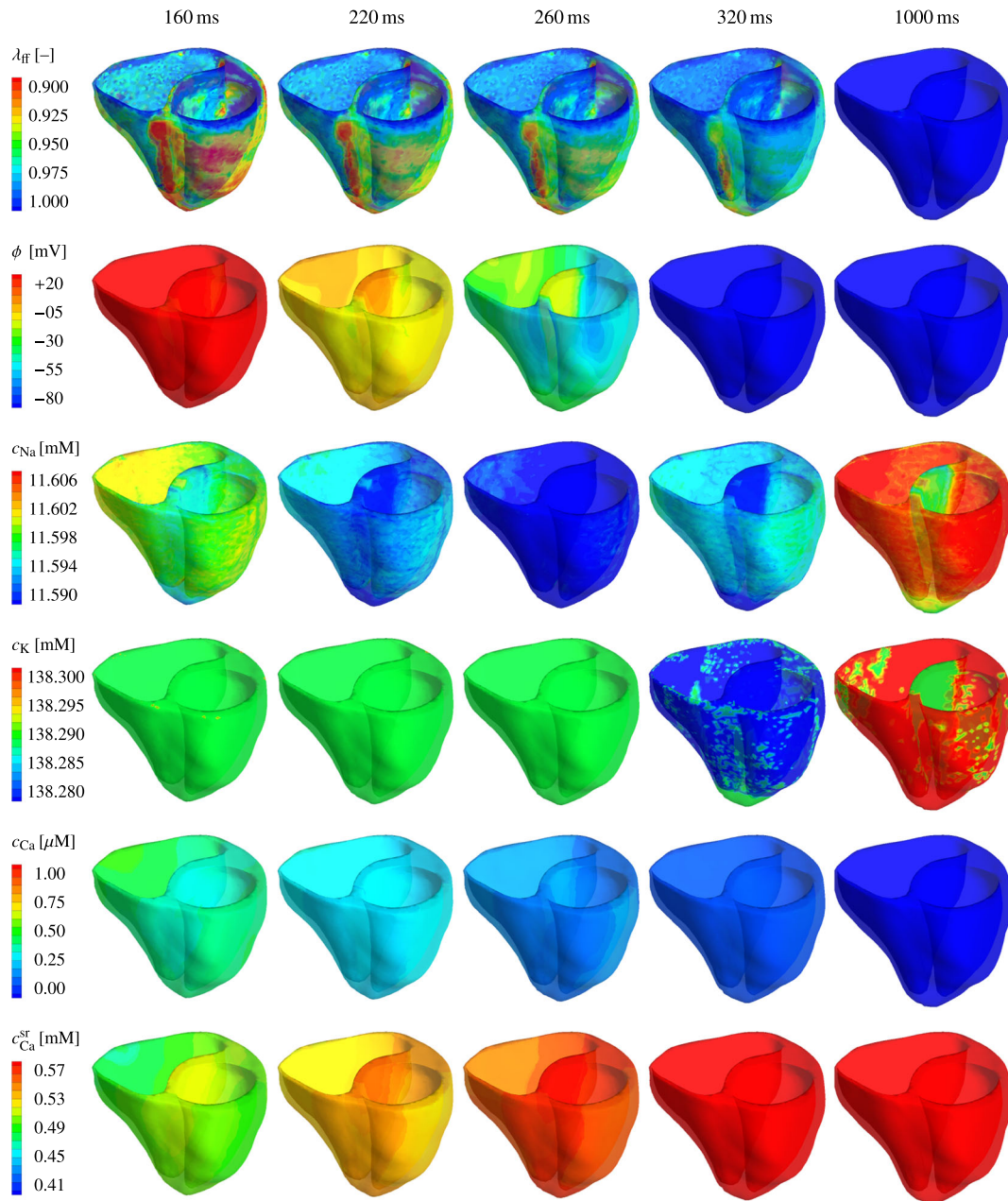


Figure 8. Chemo-electro-mechanical coupling in the human heart. Spatio-temporal evolution of the fiber contraction λ_{ff} , the transmembrane potential ϕ , the intracellular sodium, potassium, and calcium concentrations c_{Na} , c_K , and c_{Ca} and the calcium concentration in the sarcoplasmic reticulum c_{Ca}^{sr} during the gradual repolarization phase of the cardiac cycle. Changes in the individual ion concentrations initiate a slow decrease in the transmembrane potential ϕ from +20 mV to -86 mV. A decrease in the intracellular calcium concentration c_{Ca} initiates mechanical relaxation with λ_{ff} returning gradually to 0%. During the filling phase, the apex moves away from the base, and the heart undergoes a counterclockwise rotation back to its original position.

corresponding number of Newton iterations within the adaptive time-stepping scheme. The algorithm typically converges within four Newton–Raphson iterations. For more required iterations, the adaptive algorithm automatically decreases the time step size, for example, during the rapid upstroke phase before $t = 0.05$ s where the time step size becomes as small as $\Delta t = 0.03$ ms and during the repolarization phase between $t = 0.25$ s and $t = 0.32$ s where the time step size becomes as

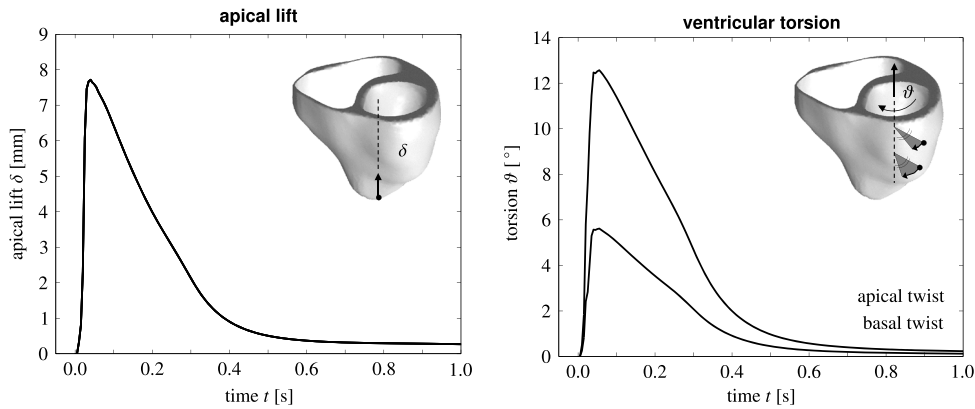


Figure 9. Mechanical contraction in the human heart. Temporal evolution of apical lift δ characterizing the vertical movement of the apex along the heart’s long axis toward the fixed base, left. Temporal evolution of ventricular torsion ϑ characterizing the rotation of two locations in the lateral left ventricular wall around the heart’s long axis, right. Shortly after the onset of excitation, the apex lifts rapidly toward the base moving upward by approximately 8 mm. Simultaneously, the heart twists rapidly about its long axis rotating clockwise by approximately 6° and 13° , with the amount of torsion increasing from the fixed base to the free apex. Both apical lift and ventricular torsion then decrease gradually as the heart returns smoothly to its resting state.

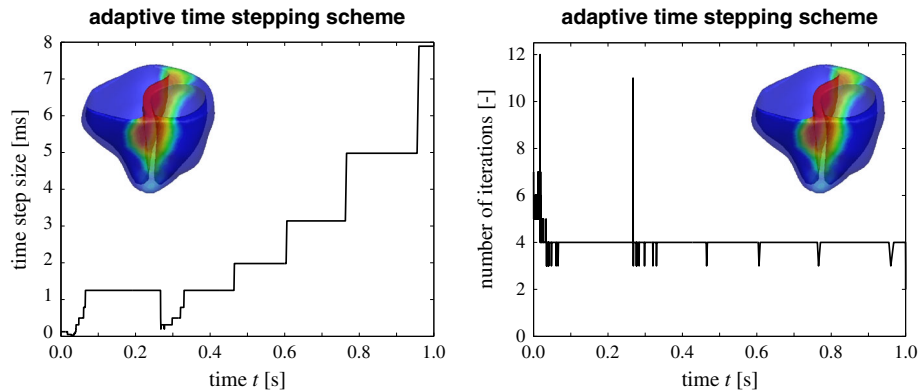


Figure 10. Algorithmic performance. Time step size and number of iterations for adaptive time-stepping scheme. The algorithm typically converges within four Newton–Raphson iterations. For more iterations, the adaptive algorithm automatically decreases the time step size, for example, during the rapid upstroke phase before $t = 0.05$ s and during the repolarization phase between $t = 0.25$ s and $t = 0.32$ s. For less iterations, the adaptive algorithm automatically increases the time step size, for example, during the plateau phase, between $t = 0.05$ s and $t = 0.25$ s and during the resting phase after $t = 0.32$ s. The total number of time increments is 1288, and the overall run time is 51.97 h, calculated on a single core of an i7-950 3.06 GHz desktop with 12 GB of memory.

small as $\Delta t = 0.31$ ms. For less required iterations, the adaptive algorithm automatically increases the time step size, for example, during the plateau phase, between $t = 0.05$ s and $t = 0.25$ s where the time step size becomes as large as $\Delta t = 1.25$ ms and during the resting phase after $t = 0.32$ s where the time step size becomes as large as $\Delta t = 7.89$ ms.

Table III confirms these observations. During the rapid upstroke phase, at $t = 0.0125$ s, the algorithm requires six Newton iterations to fully converge with the given convergence tolerance of $1.0E-09$. During the early repolarization phase, at $t = 0.050$ s, during the plateau phase, at $t = 0.125$ s, and during the resting phase, at $t = 0.750$ s, the algorithm requires only three Newton iterations. During the final repolarization phase, at $t = 0.250$ s, the algorithm requires four New-

Table III. Algorithmic performance. Characteristic quadratic convergence of global Newton–Raphson iteration, illustrated in terms of the representative residuals of the relative error during five different phases of the cardiac cycle.

	Phase 0 upstroke [0.0125 s]	Phase 1 early repolarization [0.050 ms]	Phase 2 plateau [0.125 s]	Phase 3 final repolarization [0.250 s]	Phase 4 resting state [0.750 s]
Iteration 1	1.0000E+00	1.0000E+00	1.0000E+00	1.0000E+00	1.0000E−01
Iteration 2	2.8851E−01	9.2488E−06	1.9453E−04	1.3929E−04	9.1883E−06
Iteration 3	1.5778E−02	5.1421E−11	4.8334E−10	1.6442E−09	2.8551E−10
Iteration 4	1.0136E−04	–	–	4.5720E−14	–
Iteration 5	6.8749E−08	–	–	–	–
Iteration 6	7.3132E−14	–	–	–	–

ton iterations. Overall, Table III confirms the consistent linearization of our algorithm through the quadratic convergence of the global Newton iteration during all five phases of the cardiac cycle.

We do not observe stability issues, which we attribute to the implicit nature of the underlying time integration scheme. The simulation run of an entire cardiac cycle finishes after a total number of time increments of 1288. The overall run time is 51.97 h, calculated on a single core of an i7-950 3.06 GHz desktop with 12 GB of memory.

6. DISCUSSION

We have presented a unified, fully coupled finite element formulation for chemo-electro-mechanical phenomena in living biological systems and demonstrated its potential to simulate excitation–contraction coupling in a patient-specific human heart. The novel aspect of this work is that all chemical, electrical, and mechanical fields are solved monolithically using an implicit time integration scheme, consistently linearized, embedded in a Newton–Raphson solution strategy. In contrast to most existing algorithms, the proposed discretization scheme is unconditionally stable, computationally efficient, highly modular, geometrically flexible, and easily expandable.

Unconditional stability is guaranteed by using a fully coupled, implicitly integrated, consistently linearized finite element approach. Existing algorithms are typically on the basis of sequential, staggered solution techniques [34] and utilize explicit time marching schemes [27, 31]. They are inherently unstable and limited in time step size [65], which might make them less robust and less efficient. Especially during the rapid upstroke phase, steep spatial and temporal gradients in the unknown fields might initiate spurious instabilities when using explicit time-stepping schemes [35]. To avoid these potential limitations, we have applied an implicit backward Euler time integration scheme [40, 42]. We have shown that this scheme is capable of handling sharp chemical, electrical, and mechanical profiles associated with rapid changes in the local and global unknowns. Because our algorithm follows the classical layout of nonlinear finite element schemes, we can utilize readily available adaptive time-stepping schemes at no extra cost or effort [37]. We have demonstrated that a simple, ad hoc, iteration counter-based time adaptive scheme automatically decreases the time step size during phases with steep temporal gradients and, conversely, increases the time size when all unknowns evolve smoothly.

Efficiency is increased not only by using time adaptive schemes but also by using a classical finite-element specific global–local split [38, 39]. Almost most existing algorithms discretize all unknowns globally, we only introduce four global degrees of freedom at the node point level, that is, the vector-valued mechanical deformation and the scalar-valued electrical potential. We introduce, update, and store all other state variables locally on the integration point level [30, 63, 66], that is, the 13 chemical gating variables and the four ion concentrations for our particular cardiomyocyte model. Accordingly, our global system matrix remains small and efficiently to invert during the solution procedure.

Modularity originates from the nature of the underlying finite element discretization, which introduces all cell-specific unknowns as local internal variables on the integration point level. This allows

us to modularly integrate the proposed algorithm into any commercial finite element package that can handle a coupled nonlinear system of vector-valued and scalar-valued governing equations [37]. The simplest strategy would be to use an existing thermo-mechanical element formulation and re-interpret the temperature field as the transmembrane potential. Algorithmic modifications are then restricted exclusively to the constitutive subroutine, in which we would solve the chemical problem and store the ion concentrations and gating variables as internal variables at each integration point [40]. Another natural benefit of using finite element schemes is that the modular treatment of the constitutive equations allows us to combine arbitrary cell types, for example, epicardial and endocardial ventricular cells [22, 23], Purkinje fiber cells [19], atrial cells [20], and pacemaker cells [18], to effortlessly account for microstructural inhomogeneities. We have successfully combined excitable and non-excitable cells [7], self-excitable pacemaker cells and stable ventricular cells [38], ventricular cells and Purkinje fiber cells with different conductivities [59], and ventricular cells with different action potential durations [61] to seamlessly incorporate the structural inhomogeneities of cardiac tissue.

Geometrical flexibility is probably the most advantageous feature of finite element techniques when compared with finite difference schemes or finite volume methods. Unlike existing schemes, which are most powerful on regular grids, the proposed algorithm can be applied to arbitrary geometries with arbitrary initial and boundary conditions [67]. Finite element algorithms can easily handle medical image-based patient-specific geometries [59, 68, 69]. In a simple pre-processing step, we could even utilize finite element algorithms to create fiber orientations on arbitrary patient-specific meshes using Lagrangian feature-based interpolation as illustrated in Figure 6. The key advantage of finite element algorithms, however, is that it allows us to simulate finite deformations throughout the cardiac cycle in a straightforward and natural way [42]. Finite element models inherently allow for global or local, adaptive mesh refinement to increase the accuracy of the solution [34], for example, to accurately resolve transmural gradients of the underlying activation and deactivation patterns [10].

Ease of expandability is attributed to the fact that we use a single unified discretization technique. Being finite element-based and transparent in nature, our approach lays the groundwork for a robust and stable whole heart model of excitation–contraction coupling. Through the incorporation of an additional scalar-valued global unknown, for example, to characterize the extracellular potential field, we could easily expand the proposed monodomain formulation into a more accurate bidomain formulation [43, 70, 71]. Through the incorporation of additional gating variables as local unknowns, for example, to characterize the optical manipulation of cardiac cells [5], we could easily expand the proposed formulation into a photoelectrochemical formulation [72].

In the future, we will further calibrate and validate our model across the different scales. On the cellular level, we will perform local patch clamp electrophysiology [5]; on the cell culture level, we will analyze microelectroarray recordings [7]; on the tissue level, we will perform heart slice force measurements [29]. On the organ level, we will consult large animal experiments [10] and patient-specific clinical data [59, 73]. A current trend in cardiac electromechanics is to establish valuable libraries of benchmark solutions [74, 75], against which we will compare our model both qualitatively and quantitatively in the near future. We have already validated the electrical module of our model using a patient-specific electrocardiogram extracted from the electrical flux vector \mathbf{Q} integrated over the cardiac domain [59, 61]. We have also validated the mechanical module in terms of the maximum fiber contraction λ_{ff} of approximately 10%, which agrees nicely with an earlier study in an ovine model where the maximum fiber contraction was found to lie within 8% and 10%. We plan to further validate the mechanical module in terms of the apical lift and ventricular torsion extracted from Figure 9 and ultimately, in terms of pressure–volume loops.

In summary, we believe that there are compelling reasons to consider the use of fully coupled, implicitly integrated, consistently linearized discretization strategies that enjoy the advantages inherent to finite element schemes. Initially, it may seem tedious to transition existing chemical, electrical, and mechanical algorithms into a single unified chemo-electro-mechanical algorithm. However, we are convinced that these efforts will pay off when it comes to truly predicting the impact of pharmacological, interventional, and surgical treatment options to systematically manipulate chemical, electrical, and mechanical fields in the human heart.

APPENDIX A

In this section, we specify the constitutive equations of the chemo-electrical problem for a ventricular cardiomyocyte [40]. The cell model draws on the classical Luo–Rudy model [22, 44], enhanced by several recent modifications [23, 76–78] and accounts for $n_{\text{ion}} = 4$ ion concentrations, $c_{\text{ion}} = [c_{\text{Na}}, c_{\text{K}}, c_{\text{Ca}}, c_{\text{Ca}}^{\text{sr}}]$, where c_{Na} , c_{K} and c_{Ca} are the intracellular sodium, potassium, and calcium concentrations, and $c_{\text{Ca}}^{\text{sr}}$ is the calcium concentration in the sarcoplasmic reticulum. The model contains $n_{\text{crt}} = 15$ ionic currents, $I_{\text{crt}} = [I_{\text{Na}}, I_{\text{bNa}}, I_{\text{NaK}}, I_{\text{NaCa}}, I_{\text{K1}}, I_{\text{Kr}}, I_{\text{Ks}}, I_{\text{pK}}, I_{\text{t0}}, I_{\text{CaL}}, I_{\text{bCa}}, I_{\text{pCa}}, I_{\text{leak}}, I_{\text{up}}, I_{\text{rel}}]$, as illustrated in Figure 2. The states of the channels associated with these currents are gated by $n_{\text{gate}} = 13$ gating variables, $g_{\text{gate}} = [g_{\text{m}}, g_{\text{h}}, g_{\text{j}}, g_{\text{xr1}}, g_{\text{xr2}}, g_{\text{xs}}, g_{\text{r}}, g_{\text{s}}, g_{\text{d}}, g_{\text{f}}, g_{\text{xK1}\infty}, g_{\text{rCa}}, g_{\text{g}}]$. For each ion, sodium, potassium, and calcium, we evaluate the classical Nernst equation,

$$\phi_{\text{ion}} = \frac{RT}{z_{\text{ion}}F} \log \left(\frac{c_{\text{ion0}}}{c_{\text{ion}}} \right) \quad \text{with} \quad \phi_{\text{ion}} = [\phi_{\text{Na}}, \phi_{\text{K}}, \phi_{\text{Ca}}] \quad (\text{A.1})$$

to determine the concentration-dependent reversal potential ϕ_{ion} , that is, the potential difference across the cell membrane, which would be generated by this particular ion if no other ions were present. In that case, if the membrane were permeable to this specific ion, its transmembrane potential ϕ would approach this ion's equilibrium potential ϕ_{ion} . Here, $R = 8.3143 \text{ J K}^{-1} \text{ mol}^{-1}$ is the gas constant, $T = 310 \text{ K}$ is the absolute temperature, and $F = 96.4867 \text{ C/mmole}$ is the Faraday constant. The constant z_{ion} is the elementary charge per ion. For singly charged sodium and potassium ions $z_{\text{Na}} = 1$ and $z_{\text{K}} = 1$, respectively, and for doubly charged calcium ions $z_{\text{Ca}} = 2$. The extracellular sodium, potassium, and calcium concentrations are $c_{\text{Na0}} = 140 \text{ mM}$, $c_{\text{K0}} = 5.4 \text{ mM}$, and $c_{\text{Ca0}} = 2 \text{ mM}$. We now specify the individual concentrations, currents, and gating variables for sodium, potassium, and calcium to define the source term $F\phi$ for the electrical problem (21). In what follows, we use the units milliseconds for time t , millivolts for voltage ϕ , picoamperes per picofarad for ionic currents across the cell membrane, millimolar per millisecond for ionic currents across the membrane of the sarcoplasmic reticulum, nanosiemens per picofarad for conductances C_{crt} , and millimoles per liter for intracellular and extracellular ion concentrations c_{ion} . Table I summarizes all local chemo-electrical parameters of our human ventricular cardiomyocyte model.

A.1. Sodium concentration, currents, and gating variables

Sodium plays a crucial role in generating the fast upstroke in the initial phase of the action potential. At rest, the intracellular sodium concentration is approximately $c_{\text{Na}} = 11.6 \text{ mM}$. This implies that, according to equation (A.1), the sodium equilibrium potential is $\phi_{\text{Na}} = +66.5 \text{ mV}$. Accordingly, both electrical forces and chemical gradients draw extracellular sodium ions into the cell. At rest, the influx of sodium ions is low because the membrane is relatively impermeable to sodium. An external stimulus above a critical threshold value causes the fast sodium channel to open and initiates a rapid inflow of sodium ions associated with the rapid depolarization of the cell membrane. The transmembrane potential increases rapidly by more than 100 mV in less than 2 ms, see Figure 3. At the end of the upstroke, the cell membrane is positively charged, and the fast sodium channels return to their closed state. In our specific cell model, the sodium concentration

$$\dot{c}_{\text{Na}} = -\frac{C}{VF} [I_{\text{Na}} + I_{\text{bNa}} + 3 I_{\text{NaK}} + 3 I_{\text{NaCa}}] \quad (\text{A.2})$$

is evolving in response to the fast sodium current I_{Na} , the background sodium current I_{bNa} , the sodium potassium pump current I_{NaK} , and the sodium calcium exchanger current I_{NaCa} according to Faraday's law of electrolysis. The membrane capacitance per unit surface area is $C = 185 \text{ pF}$, the cytoplasmic volume is $V = 16,404 \text{ }\mu\text{m}^3$, and the Faraday constant is $F = 96.4867 \text{ C/mmole}$. Both the sodium potassium pump and sodium calcium exchanger operate at a three-to-two ratio as

indicated by the scaling factor of 3. The sodium related currents are functions of the transmembrane potential ϕ , the gating variables g_{gate} , and the ion concentrations c_{ion} ,

$$\begin{aligned}
 I_{\text{Na}} &= C_{\text{Na}}^{\text{max}} g_m^3 g_h g_j [\phi - \phi_{\text{Na}}] \\
 I_{\text{bNa}} &= C_{\text{bNa}}^{\text{max}} [\phi - \phi_{\text{Na}}] \\
 I_{\text{NaK}} &= I_{\text{NaK}}^{\text{max}} [c_{\text{K0}}c_{\text{Na}}] [(c_{\text{Na}} + c_{\text{NaK}})[c_{\text{K0}} + c_{\text{KNa}}] \\
 &\quad [1 + 0.1245e^{-0.1\phi F/RT} + 0.0353e^{-\phi F/RT}]^{-1} \\
 I_{\text{NaCa}} &= I_{\text{NaCa}}^{\text{max}} \left[e^{\gamma\phi F/RT} c_{\text{Na}}^3 c_{\text{Ca0}} - e^{(\gamma-1)\phi F/RT} c_{\text{Na0}}^3 c_{\text{Ca}} \gamma_{\text{NaCa}} \right] \\
 &\quad \left[[c_{\text{NaCa}}^3 + c_{\text{Na0}}^3] [c_{\text{CaNa}} + c_{\text{Ca0}}] \left[1 + k_{\text{NaCa}}^{\text{sat}} e^{(\gamma-1)\phi F/RT} \right] \right]^{-1}.
 \end{aligned} \tag{A.3}$$

Here, the scaling factors are the maximum fast sodium conductance $C_{\text{Na}}^{\text{max}} = 14.838$ nS/pF, maximum background sodium conductance $C_{\text{bNa}}^{\text{max}} = 0.00029$ nS/pF, maximum sodium potassium pump current $I_{\text{NaK}}^{\text{max}} = 1.362$ pA/pF, and maximum sodium calcium exchanger current $I_{\text{NaCa}}^{\text{max}} = 1000$ pA/pF. The rapid upstroke in the membrane potential is generated by the fast sodium current I_{Na} , characterized through a three-gate formulation of Beeler–Reuter type [21] in terms of the sodium activation gate g_m , fast sodium inactivation gate g_h , and slow sodium inactivation gate g_j . The gating variables follow classical Hodgkin–Huxley type equations (24) of the format $\dot{g}_{\text{gate}} = [g_{\text{gate}}^{\infty} - g_{\text{gate}}] / \tau_{\text{gate}}$. Here, g_{gate}^{∞} characterizes the steady-state value, and τ_{gate} denotes the time constant associated with reaching the steady state. For the sodium activation gate $\dot{g}_m = [g_m^{\infty} - g_m] / \tau_m$, which initiates the rapid upstroke, they take the following explicit representations

$$\begin{aligned}
 g_m^{\infty} &= [1 + e^{(-56.86-\phi)/9.03}]^{-2} \\
 \tau_m &= 0.1 [1 + e^{(-60-\phi)/5}]^{-1} \left[[1 + e^{(\phi+35)/5}]^{-1} + [1 + e^{(\phi-50)/200}]^{-1} \right].
 \end{aligned} \tag{A.4}$$

For the fast sodium inactivation gate $\dot{g}_h = [g_h^{\infty} - g_h] / \tau_h$, which initiates a fast inactivation of the sodium channel almost instantaneously after the rapid upstroke, the steady-state value and the corresponding time constant take the following forms

$$\begin{aligned}
 g_h^{\infty} &= [1 + e^{(\phi+71.55)/7.43}]^{-2} \\
 \tau_h &= \begin{cases} 0.1688 [1 + e^{-(\phi+10.66)/11.1}] & \text{if } \phi \geq -40 \\ [0.057 e^{-(\phi+80)/6.8} + 2.7 e^{0.079\phi} + 3.1 \cdot 10^5 e^{0.3485\phi}]^{-1} & \text{if } \phi < -40. \end{cases}
 \end{aligned} \tag{A.5}$$

For the slow sodium inactivation gate $\dot{g}_j = [g_j^{\infty} - g_j] / \tau_j$, which gradually inactivates the fast sodium channel over a time span of 100–200 ms, the Hodgkin–Huxley constants take the following form

$$\begin{aligned}
 g_j^{\infty} &= [1 + e^{(\phi+71.55)/7.43}]^{-2} \\
 \tau_j &= [\alpha_j + \beta_j]^{-1} \\
 \alpha_j &= \begin{cases} 0 & \text{if } \phi \geq -40 \\ [-2.5428 \cdot 10^4 e^{0.2444\phi} - 6.948 \cdot 10^{-6} e^{-0.04391\phi}] & \\ [\phi + 37.78] [1 + e^{0.311(\phi+79.23)}]^{-1} & \text{if } \phi < -40 \end{cases} \\
 \beta_j &= \begin{cases} 0.6 e^{0.057\phi} [1 + e^{-0.1(\phi+32)}]^{-1} & \text{if } \phi \geq -40 \\ 0.02424 e^{-0.01052\phi} [1 + e^{-0.1378(\phi+40.14)}]^{-1} & \text{if } \phi < -40. \end{cases}
 \end{aligned} \tag{A.6}$$

The sodium ions that enter the cell rapidly during the fast upstroke are removed from the cell by the sodium potassium pump I_{NaK} , a metabolic pump that continuously expels sodium ions from the cell interior and pumps in potassium ions. The intracellular sodium concentration is further affected by expulsion of intracellular calcium ions through sodium calcium exchange I_{NaCa} . The additional parameters for the sodium potassium pump current I_{NaK} and for the sodium calcium exchanger current I_{NaCa} are the extracellular sodium, potassium, and calcium concentrations $c_{\text{Na}0} = 140$ mM, $c_{\text{K}0} = 5.4$ mM, and $c_{\text{Ca}0} = 2$ mM, the half saturation constants $c_{\text{CaNa}} = 1.38$ mM, $c_{\text{NaCa}} = 87.5$ mM, $c_{\text{KNa}} = 1$ mM, $c_{\text{NaK}} = 40$ mM, the sodium calcium saturation factor $k_{\text{NaCa}}^{\text{sat}} = 0.1$, the outward sodium calcium pump current enhancing factor $\gamma_{\text{NaCa}} = 2.5$, and the voltage dependent sodium calcium parameter $\gamma = 0.35$.

A.2. Potassium concentration, currents, and gating variables

Potassium plays an important role in maintaining the appropriate action potential profile in all four phases after the rapid upstroke. At rest, the intracellular potassium concentration is typically about $c_{\text{K}} = 138.3$ mM, and the related equilibrium potential is $\phi_{\text{K}} = -86.6$ mV according to equation (A.1). This value is very close to, but slightly more negative than, the resting potential of $\phi = -86$ mV actually measured in ventricular cardiomyocytes. Unlike for sodium, the electrical force that pulls potassium ions inward is slightly weaker than the chemical force of diffusion pulling potassium ions outward. This implies that potassium tends to leave the resting cell. At the end of the rapid upstroke, before the beginning of the plateau, we observe an early, brief period of limited repolarization governed by the voltage-activated transient outward current I_{t0} . The following plateau phase is dominated by an influx of calcium ions which is balanced by the efflux of an equal amount of positively charged potassium ions, mainly regulated by the rapid and slow delayed rectifier currents I_{Kr} and I_{Ks} . The final repolarization phase can almost exclusively be attributed to potassium ions leaving the cell such that the membrane potential can return to its resting state, see Figure 3. In summary, the evolution of the potassium concentration

$$\dot{c}_{\text{K}} = -\frac{C}{VF} [I_{\text{K1}} + I_{\text{Kr}} + I_{\text{Ks}} - 2I_{\text{NaK}} + I_{\text{pK}} + I_{\text{t0}} + I_{\text{stim}}] \quad (\text{A.7})$$

is mainly controlled by four currents, the inward rectifier current I_{K1} , the rapid delayed rectifier current I_{Kr} , the slow delayed rectifier current I_{Ks} , and the transient outward current I_{t0} . Moreover, it is affected by the sodium potassium pump current I_{NaK} and the plateau potassium current I_{pK} . Currents are scaled by the membrane capacitance per unit surface area $C = 185$ pF, the cytoplasmic volume $V = 16404 \mu\text{m}^3$, and the Faraday constant $F = 96.4867$ C/mmol. The individual potassium related currents take the following forms

$$\begin{aligned} I_{\text{K1}} &= C_{\text{K1}}^{\text{max}} g_{\text{K1}}^{\infty} [c_{\text{K}0}/5.4]^{1/2} [\phi - \phi_{\text{K}}] \\ I_{\text{Kr}} &= C_{\text{Kr}}^{\text{max}} g_{\text{xr1}} g_{\text{xr2}} [c_{\text{K}0}/5.4]^{1/2} [\phi - \phi_{\text{K}}] \\ I_{\text{Ks}} &= C_{\text{Ks}}^{\text{max}} g_{\text{xs}}^2 [\phi - \phi_{\text{Ks}}] \\ I_{\text{NaK}} &= I_{\text{NaK}}^{\text{max}} [c_{\text{K}0}c_{\text{Na}}] \left[[c_{\text{Na}} + c_{\text{NaK}}][c_{\text{K}0} + c_{\text{KNa}}] \right. \\ &\quad \left. [1 + 0.1245e^{-0.1\phi F/RT} + 0.0353e^{-\phi F/RT}] \right]^{-1} \\ I_{\text{pK}} &= C_{\text{pK}}^{\text{max}} \left[1 + e^{[25-\phi]/5.98} \right]^{-1} [\phi - \phi_{\text{K}}] \\ I_{\text{t0}} &= C_{\text{t0}}^{\text{max}} g_{\text{r}} g_{\text{s}} [\phi - \phi_{\text{K}}], \end{aligned} \quad (\text{A.8})$$

where the individual scaling factors are the maximum inward rectifier conductance $C_{\text{K1}}^{\text{max}} = 5.405$ nS/pF, maximum rapid delayed rectifier conductance $C_{\text{Kr}}^{\text{max}} = 0.096$ nS/pF, maximum slow delayed rectifier conductance for epicardial and endocardial cells $C_{\text{Ks,epi}}^{\text{max}} = C_{\text{Ks,endo}}^{\text{max}} = 0.245$ nS/pF and for M cells $C_{\text{Ks,M}}^{\text{max}} = 0.062$ nS/pF, maximum sodium potassium pump current $I_{\text{NaK}}^{\text{max}} = 1.362$ pA/pF, maximum potassium pump conductance $C_{\text{pK}}^{\text{max}} = 0.0146$ nS/pF, and maximum transient outward conductance for epicardial and M cells $C_{\text{t0,epi}}^{\text{max}} = C_{\text{t0,M}}^{\text{max}} = 0.294$ nS/pF and for

endocardial cells $C_{t0,endo}^{max} = 0.073$ nS/pF. The maximum inward rectifier current I_{K1} , which is most active during the later phases of the action potential, depends explicitly on the extracellular potassium concentration $c_{K0} = 5.4$ mM. It further depends on the time-independent inward rectification factor g_{K1}^∞ parameterized in terms of the potential equilibrium potential ϕ_K given in equation (A.1)

$$\begin{aligned} g_{K1}^\infty &= \alpha_{K1} [\alpha_{K1} + \beta_{K1}]^{-1} \\ \alpha_{K1} &= 0.1 \left[1 + e^{0.06(\phi - \phi_K - 200)} \right]^{-1} \\ \beta_{K1} &= \left[3 e^{0.0002(\phi - \phi_K + 100)} + e^{0.1(\phi - \phi_K - 10)} \right] \left[1 + e^{-0.5(\phi - \phi_K)} \right]^{-1}. \end{aligned} \tag{A.9}$$

The plateau of the transmembrane potential is generated by an influx of charged calcium ions balanced by the efflux of potassium ions. The latter is governed by the rapid and slow delayed rectifier current I_{Kr} and I_{Ks} . The channel for the rapid delayed rectifier current I_{Kr} is gated by an activation gate $\dot{g}_{x1} = [g_{x1}^\infty - g_{x1}] / \tau_{x1}$ with the steady-state value and time constant given as

$$\begin{aligned} g_{xr1}^\infty &= \left[1 + e^{(-26 - \phi)/7} \right]^{-1} \\ \tau_{xr1} &= 2700 \left[1 + e^{(-45 - \phi)/10} \right]^{-1} \left[1 + e^{(\phi + 30)/11.5} \right]^{-1} \end{aligned} \tag{A.10}$$

and by an inactivation gate $\dot{g}_{x2} = [g_{x2}^\infty - g_{x2}] / \tau_{x2}$, with the following steady-state value and time constant.

$$\begin{aligned} g_{xr2}^\infty &= \left[1 + e^{(\phi + 88)/24} \right]^{-1} \\ \tau_{xr2} &= 3.36 \left[1 + e^{(-60 - \phi)/20} \right]^{-1} \left[1 + e^{(\phi - 60)/20} \right]^{-1}. \end{aligned} \tag{A.11}$$

The channel for the slow delayed rectifier current I_{Ks} is a function of the reversal potential $\phi_{Ks} = RT/F \log ([c_{K0} + p_{KNa} c_{Na0}] [c_K + p_{KNa} c_{Na}]^{-1})$ parameterized in terms of its permeability to sodium ions $p_{KNa} = 0.03$. It is gated by an activation gate $\dot{g}_{xs} = [g_{xs}^\infty - g_{xs}] / \tau_{xs}$ in terms of the following parameterization,

$$\begin{aligned} g_{xs}^\infty &= \left[1 + e^{(-5 - \phi)/14} \right]^{-1} \\ \tau_{xs} &= 1100 \left[1 + e^{(-10 - \phi)/6} \right]^{-1/2} \left[1 + e^{(\phi - 60)/20} \right]^{-1}. \end{aligned} \tag{A.12}$$

The transient potassium outward current I_{t0} is responsible for the transition between the rapid upstroke and plateau phase, where it generates an early short period of limited repolarization. It is gated by a voltage-dependent activation gate g_r with $\dot{g}_r = [g_r^\infty - g_r] / \tau_r$ defined through the following steady-state value and time constant,

$$\begin{aligned} g_r^\infty &= \left[1 + e^{(20 - \phi)/6} \right]^{-1} \\ \tau_r &= 9.5 e^{-(\phi + 40)^2/1800} + 0.8, \end{aligned} \tag{A.13}$$

and by the voltage-dependent inactivation gate g_s with $\dot{g}_s = [g_s^\infty - g_s] / \tau_s$ with the steady-state value and time constant given as follows,

$$\begin{aligned} g_s^\infty &= \left[1 + e^{(\phi + 20)/5} \right] \\ \tau_s &= 85 e^{-(\phi + 45)^2/320} + 5 \left[1 + e^{(\phi - 20)/5} \right] + 3 \end{aligned} \left. \vphantom{\begin{aligned} g_s^\infty \\ \tau_s \end{aligned}} \right\} \text{epicardium} \tag{A.14}$$

$$\begin{aligned} g_s^\infty &= \left[1 + e^{(\phi + 28)/5} \right] \\ \tau_s &= 1000 e^{-(\phi + 67)^2/1000} + 8. \end{aligned} \left. \vphantom{\begin{aligned} g_s^\infty \\ \tau_s \end{aligned}} \right\} \text{endocardium}$$

This voltage-dependent potassium inactivation gate displays a significantly different behavior for epicardial and endocardial cells and is therefore characterized differently for the individual cell types. Similar to the previous subsection, we have introduced the extracellular sodium and potassium concentrations $c_{\text{Na}0} = 140$ mM and $c_{\text{K}0} = 5.4$ mM and the half saturation constants $c_{\text{KNa}} = 1$ mM and $c_{\text{NaK}} = 40$ mM.

A.3. Calcium concentration, currents, and gating variables

Calcium is the key player to translate electrical excitation into mechanical contraction. With a typical intracellular resting concentrations of $c_{\text{Ca}} = 0.08$ μM , its equilibrium potential of $\phi_{\text{Ca}} = +135.3$ mV is much larger than the resting potential. During the plateau of the action potential, calcium ions enter the cell through calcium channels that typically activate and inactivate much more slowly than the fast sodium channels. The influx of positively charged calcium ions through the L-type calcium channel I_{CaL} is balanced by an efflux of positively charged potassium ions. The letter *L* is meant to indicate the long lasting nature of the inward calcium current. Overall, changes in the intracellular calcium concentration

$$\dot{c}_{\text{Ca}} = \gamma_{\text{Ca}} \left[-\frac{C}{2VF} [I_{\text{CaL}} + I_{\text{bCa}} + I_{\text{pCa}} - 2 I_{\text{NaCa}}] + I_{\text{leak}} - I_{\text{up}} + I_{\text{rel}} \right] \quad (\text{A.15})$$

are affected by the L-type calcium current I_{CaL} , background calcium current I_{bCa} , plateau calcium current I_{pCa} , and sodium calcium pump current I_{NaCa} , weighted by the membrane capacitance per unit surface area $C = 185$ pF, the cytoplasmic volume $V = 16,404$ μm^3 , and the Faraday constant $F = 96.4867$ C/mmol. In addition, the intracellular calcium concentration is affected by a calcium loss to the sarcoplasmic reticulum characterized through the leakage current I_{leak} , sarcoplasmic reticulum uptake current I_{up} , and sarcoplasmic reticulum release current I_{rel} . The individual calcium related currents are defined as follows:

$$\begin{aligned} I_{\text{CaL}} &= C_{\text{CaL}}^{\text{max}} [g_{\text{d}} g_{\text{f}} g_{\text{fCa}} [4\phi F^2]/[RT]] \\ &\quad \left[[c_{\text{Ca}} e^{2\phi F/[RT]} - 0.341 c_{\text{Ca}0}] [e^{2\phi F/[RT]} - 1] \right]^{-1} \\ I_{\text{bCa}} &= C_{\text{bCa}}^{\text{max}} [\phi - \phi_{\text{Ca}}] \\ I_{\text{pCa}} &= C_{\text{pCa}}^{\text{max}} c_{\text{Ca}} [c_{\text{pCa}} + c_{\text{Ca}}]^{-1} \\ I_{\text{NaCa}} &= I_{\text{NaCa}}^{\text{max}} \left[e^{\gamma\phi F/RT} c_{\text{Na}}^3 c_{\text{Ca}0} - e^{(\gamma-1)\phi F/RT} c_{\text{Na}0}^3 c_{\text{Ca}} \gamma_{\text{NaCa}} \right] \\ &\quad \left[[c_{\text{NaCa}}^3 + c_{\text{Na}0}^3] [c_{\text{CaNa}} + c_{\text{Ca}0}] [1 + k_{\text{NaCa}}^{\text{sat}} e^{(\gamma-1)\phi F/RT}] \right]^{-1} \\ I_{\text{leak}} &= I_{\text{leak}}^{\text{max}} [c_{\text{Ca}}^{\text{sr}} - c_{\text{Ca}}] \\ I_{\text{up}} &= I_{\text{up}}^{\text{max}} [1 + c_{\text{up}}^2/c_{\text{Ca}}^2]^{-1} \\ I_{\text{rel}} &= I_{\text{rel}}^{\text{max}} g_{\text{d}} g_{\text{g}} \left[1 + \gamma_{\text{rel}} c_{\text{Ca}}^{\text{sr}2} [c_{\text{rel}}^2 + c_{\text{Ca}}^{\text{sr}2}]^{-1} \right], \end{aligned} \quad (\text{A.16})$$

where the individual scaling factors are the maximum calcium conductance $C_{\text{CaL}}^{\text{max}} = 0.175$ $\text{mm}^3 \mu\text{F}^{-1} \text{s}^{-1}$, maximum background calcium conductance $C_{\text{bCa}}^{\text{max}} = 0.000592$ nS/pF, maximum plateau calcium conductance $C_{\text{pCa}}^{\text{max}} = 0.825$ nS/pF, maximum sodium calcium pump current $I_{\text{NaCa}}^{\text{max}} = 1000$ pA/pF, maximum leakage current $I_{\text{leak}}^{\text{max}} = 0.08$ s^{-1} , maximum sarcoplasmic reticulum calcium uptake current $I_{\text{up}}^{\text{max}} = 0.000425$ mM/ms, and maximum sarcoplasmic reticulum calcium release current $I_{\text{rel}}^{\text{max}} = 8.232$ mM/s. The major calcium channel, the long-lasting L-type calcium channel I_{CaL} , is controlled by the voltage-dependent activation gate $g_{\text{d}} = [g_{\text{d}}^{\infty} - g_{\text{d}}]/\tau_{\text{g}}$ characterized through the following steady-state value and time constant

$$\begin{aligned} g_{\text{d}}^{\infty} &= [1 + e^{(-5-\phi)/7.5}]^{-1} \\ \tau_{\text{d}} &= [1.4 [1 + e^{(-35-\phi)/13}]^{-1} + 0.25] [1.4 [1 + e^{(\phi+5)/5}] + [1 + e^{(50-\phi)/20}]], \end{aligned} \quad (\text{A.17})$$

by the voltage-dependent inactivate gate $\dot{g}_f = [g_f^\infty - g_f] / \tau_f$ characterized through

$$\begin{aligned} g_f^\infty &= \left[1 + e^{(\phi+20)/7} \right]^{-1} \\ \tau_f &= 1125 e^{-(\phi+27)^2/240} + 165 \left[1 + e^{(25-\phi)/10} \right]^{-1} + 80, \end{aligned} \quad (\text{A.18})$$

and by the intracellular calcium dependent inactivation gate $\dot{g}_{fCa} = [g_{fCa}^\infty - g_{fCa}] / \tau_{fCa}$ characterized through

$$\begin{aligned} g_{fCa}^\infty &= 0.685 \left[\left[1 + (c_{Ca}/0.000325)^8 \right]^{-1} + 0.1 \left[1 + e^{(c_{Ca}-0.0005)/0.0001} \right]^{-1} \right. \\ &\quad \left. + 0.2 \left[1 + e^{(c_{Ca}-0.00075)/0.0008} \right]^{-1} + 0.23 \right] \\ \tau_{fCa} &= \begin{cases} \infty & \text{if } g_{fCa}^\infty > g_{fCa} \text{ and } \phi \geq -60\text{mV} \\ 2 \text{ ms} & \text{otherwise.} \end{cases} \end{aligned} \quad (\text{A.19})$$

Accordingly, the steady-state response g_{fCa}^∞ has a switch-like shape when going from no inactivation to considerable but incomplete inactivation, depending mildly on the calcium concentration c_{Ca} for suprathreshold concentrations. Last, the calcium-induced calcium release current I_{rel} is characterized through the activation gate g_d , the same gate that is also activating the L-type calcium channel of I_{CaL} , and through the calcium-dependent inactivation gate $\dot{g}_g = [g_g^\infty - g_g] / \tau_g$ characterized through the following steady-state value and time constant,

$$\begin{aligned} g_g^\infty &= \begin{cases} \left[1 + c_{Ca}^6/0.00035^6 \right]^{-1} & \text{if } c_{Ca} \leq 0.00035 \\ \left[1 + c_{Ca}^{16}/0.00035^{16} \right]^{-1} & \text{otherwise} \end{cases} \\ \tau_g &= \begin{cases} \infty & \text{if } g_g^\infty > g_g \text{ and } \phi \geq -60\text{mV} \\ 2 \text{ ms} & \text{otherwise.} \end{cases} \end{aligned} \quad (\text{A.20})$$

The remaining parameters governing the response of the plateau calcium current I_{pCa} , calcium uptake current I_{up} , and sarcoplasmic reticulum calcium release current I_{rel} are the half saturation constants for the plateau calcium concentration $c_{pCa} = 0.0005$ mM, sarcoplasmic reticulum calcium uptake $c_{up} = 0.00025$ mM, and sarcoplasmic reticulum calcium release $c_{rel} = 0.25$ mM, respectively. The parameter $\gamma_{NaCa} = 2.5$ has been introduced to enhance the outward nature of the sodium calcium pump current I_{NaCa} . The additional parameter $\gamma_{rel} = 2$ weighs the relative influence of the sarcoplasmic reticulum calcium concentration on sarcoplasmic reticulum calcium release I_{rel} . Finally, we take into account that the total intracellular calcium concentration $c_{Ca}^{tot} = c_{Ca} + c_{Ca}^{buf}$ in the cytoplasm is the sum of the free intracellular calcium concentration c_{Ca} and the buffered calcium concentration $c_{Ca}^{buf} = [c_{Ca} c_{Ca}^{tot} / c_{Ca}^{buf}] [c_{Ca} - c_{Ca}^{buf}]^{-1}$. The definition of the free intracellular calcium concentration in equation (A.15) is therefore weighted by the parameter $\gamma_{Ca} = [1 + [c_{tot} c_{buf}] [c_{Ca} + c_{buf}]^{-2}]^{-1}$, where $c_{tot} = 0.15$ mM and $c_{buf} = 0.001$ mM are the total and half saturation cytoplasmic calcium buffer concentrations, respectively.

A.4. Sarcoplasmic reticulum calcium concentration, currents, and gating variables

The specification of the sarcoplasmic reticulum calcium concentration

$$\dot{c}_{Ca}^{sr} = \gamma_{Ca}^{sr} \frac{V}{V^{sr}} [-I_{leak} + I_{up} - I_{rel}] \quad (\text{A.21})$$

is now relatively straightforward because it mimics the corresponding loss of intracellular calcium characterized. However, now, we scale it by the ratio between the volume of the cytoplasm $V = 16404 \mu\text{m}^3$ and the volume of the sarcoplasmic reticulum $V^{sr} = 1094 \mu\text{m}^3$ to account for

differences in chemical concentrations due to ionic flux. The leakage current I_{leak} , sarcoplasmic reticulum uptake current I_{up} , and sarcoplasmic reticulum release current I_{rel} are defined as before

$$\begin{aligned} I_{\text{leak}} &= I_{\text{leak}}^{\max} [c_{\text{Ca}}^{\text{sr}} - c_{\text{Ca}}] \\ I_{\text{up}} &= I_{\text{up}}^{\max} \left[1 + c_{\text{up}}^2 / c_{\text{Ca}}^2 \right]^{-1} \\ I_{\text{rel}} &= I_{\text{rel}}^{\max} g_d g_g \left[1 + \gamma_{\text{rel}} c_{\text{Ca}}^{\text{sr}2} [c_{\text{rel}}^2 + c_{\text{Ca}}^{\text{sr}2}]^{-1} \right]. \end{aligned} \quad (\text{A.22})$$

The maximum leakage current $I_{\text{leak}}^{\max} = 0.08 \text{ s}^{-1}$, maximum sarcoplasmic reticulum calcium uptake current $I_{\text{up}}^{\max} = 0.000425 \text{ mM/ms}$, maximum sarcoplasmic reticulum calcium release current $I_{\text{rel}}^{\max} = 8.232 \text{ mM/s}$, the half saturation constants for the calcium uptake $c_{\text{up}} = 0.00025 \text{ mM}$ and for the calcium release $c_{\text{rel}} = 0.25 \text{ mM}$ and the weighting coefficient $\gamma_{\text{rel}} = 2$ have already been introduced in the previous subsection. Similar to the previous subsection, we need to take into account that the total calcium concentration in the sarcoplasmic reticulum $c_{\text{Ca}}^{\text{sr} \text{tot}} = c_{\text{Ca}}^{\text{sr}} + c_{\text{Ca}}^{\text{sr} \text{buf}}$ is the sum of the free sarcoplasmic reticulum calcium concentration $c_{\text{Ca}}^{\text{sr}}$ and the buffered sarcoplasmic reticulum calcium concentration $c_{\text{Ca}}^{\text{sr} \text{buf}} = [c_{\text{Ca}}^{\text{sr}} c_{\text{tot}}^{\text{sr}}] [c_{\text{Ca}}^{\text{sr}} - c_{\text{buf}}^{\text{sr}}]^{-1}$. The definition of the free sarcoplasmic reticulum calcium concentration in equation (A.21) is therefore weighted by the parameter $\gamma_{\text{Ca}}^{\text{sr}} = \left[1 + [c_{\text{tot}}^{\text{sr}} c_{\text{buf}}^{\text{sr}}] [c_{\text{Ca}}^{\text{sr}} + c_{\text{buf}}^{\text{sr}}]^{-2} \right]^{-1}$, where $c_{\text{tot}}^{\text{sr}} = 10 \text{ mM}$ and $c_{\text{buf}}^{\text{sr}} = 0.3 \text{ mM}$ are the total and half saturation sarcoplasmic reticulum calcium buffer concentrations, respectively.

ACKNOWLEDGEMENTS

This study was supported by the Biomedical Computation Graduate Training Grant 5T32GM063495 and the Sang Samuel Wang Stanford Graduate Fellowship to Jonathan Wong and by the National Science Foundation CAREER award CMMI 0952021, the National Science Foundation INSPIRE grant 1233054, and the National Institutes of Health grant U54GM072970 to Ellen Kuhl, and through the European Union Seventh Framework Programme (FP7/2007-2013) under Grant PCIG09-GA-2011-294161 to Serdar Göktepe.

REFERENCES

1. Braunwald E. *Heart Disease: A Textbook of Cardiovascular Medicine*. W.B Saunders Co: Philadelphia, 1997.
2. American Heart Association. *Heart Disease and Stroke Statistics -2012 Update*. American Heart Association: Dallas, Texas.
3. Hunt SA, Abraham WT, Chin MH, Feldman AM, Francis GS, Ganiats TG, Jessup M, Konstam MA, Mancini DM, Michl K, Oates JA, Rahko PS, Silver MA, Stevenson LW, Yancy CW, Antman EM, Smith SC, Adams CD, Anderson JL, Faxon DP, Fuster V, Halperin JL, Hiratzka LF, Jacobs AK, Nishimura R, Ornato JP, Page RL, Riegel B. ACC/AHA 2005 Guideline update for the diagnosis and management of chronic heart failure in the adult. *Circulation* 2005; **112**:e154–235.
4. Nordsletten DA, Yankama B, Umeton R, Ayyadurai VAS, Dewey C. Multiscale mathematical modeling to support drug development. *IEEE Transactions on Biomedical Engineering* 2011; **58**:3508–3512.
5. Abilez OJ, Wong J, Prakash R, Deisseroth K, Zarins CK, Kuhl E. Multiscale computational models for optogenetic control of cardiac function. *Biophysical Journal* 2011; **101**:1326–1334.
6. Hamill OP, Marty A, Neher E, Sakmann B, Sigworth FJ. Improved patch-clamp techniques for high-resolution current recording from cells and cell-free membrane patches. *Pflügers Archiv-European Journal of Physiology* 1981; **391**:85–100.
7. Chen MQ, Wong J, Kuhl E, Giovangrandi L, Kovacs GTA. Characterization of electrophysiological conduction in cardiomyocyte co-cultures using co-occurrence analysis. *Computer Methods in Biomechanics and Biomedical Engineering* 2013; **16**:185–197.
8. Thomas C, Springer P, Loeb G, Berwald-Netter Y, Okun L. A miniature microelectrode array to monitor the bioelectric activity of cultured cells. *Experimental Cell Research* 1972; **74**:61–66.
9. Itoh A, Krishnamurthy G, Swanson J, Ennis D, Bothe W, Kuhl E, Karlsson M, Davis L, Miller DC, Ingels NB. Active stiffening of mitral valve leaflets in the beating heart. *American Journal of Physiology-Heart and Circulatory Physiology* 2009; **296**:H1766–H1773.
10. Tsamis A, Bothe W, Kvitting J, Swanson J, Miller D, Kuhl E. Active contraction of cardiac muscle: In vivo characterization of mechanical activation sequences in the beating heart. *Journal of the Mechanical Behavior of Biomedical Materials* 2011; **4**:1167–1176.
11. Bers MD. *Excitation-Contraction Coupling and Cardiac Contractile Force*. Kluwer Academic Publishers: Dordrecht, 2001.

12. Böhl M, Reese S, Parker KK, Kuhl E. Computational modeling of muscular thin films for cardiac repair. *Computational Mechanics* 2009; **43**:535–544.
13. Opie LH. *Heart Physiology: From Cell to Circulation*. Lippincott Williams & Wilkins: Philadelphia, 2003.
14. Fink M, Niederer SA, Cherry EM, Fenton FH, Koivumäki JT, Seemann G, Thul R, Zhang H, Sachse FB, Beard D, Crampin EJ, Smith NP. Cardiac cell modeling: observations from the heart of the cardiac physiome project. *Progress in Biophysics and Molecular Biology* 2011; **104**:2–21.
15. Hodgkin AL, Huxley AF. A quantitative description of membrane current and its application to conductance and excitation in nerve. *Journal of Physiology* 1952; **117**:500–544.
16. FitzHugh R. Impulses and physiological states in theoretical models of nerve membranes. *Biophysical Journal* 1961; **1**:445–466.
17. Nagumo J, Arimoto S, Yoshizawa S. Active pulse transmission line simulating nerve axon. *Proceedings of the Institute of Radio Engineers* 1962; **50**:2061–2070.
18. Noble D. A modification of the Hodgkin–Huxley equations applicable to Purkinje fibre action and pacemaker potentials. *Journal of Physiology* 1962; **160**:317–352.
19. McAllister RE, Noble D, Tsien RW. Reconstruction of the electrical activity of cardiac Purkinje fibres. *Journal of Physiology* 1975; **251**:1–59.
20. Courtemanche M, Ramirez RJ, Nattel S. Ionic mechanisms underlying human atrial action potential properties: insights from a mathematical model. *American Journal of Physiology-Heart and Circulatory Physiology* 1998; **275**:301–321.
21. Beeler GW, Reuter H. Reconstruction of the action potential of ventricular myocardial fibers. *Journal of Physiology* 1977; **268**:177–210.
22. Luo CH, Rudy Y. A model of the ventricular cardiac action potential: depolarization, repolarization, and their changes. *Circulation Research* 1991; **68**:1501–1526.
23. ten Tusscher KHWJ, Noble D, Noble P, Panfilov A. A model for human ventricular cardiomyocytes. *American Journal of Physiology-Heart and Circulatory Physiology* 2004; **286**:H1573–H1589.
24. Aliev RR, Panfilov AV. A simple two-variable model of cardiac excitation. *Chaos, Solitons and Fractals* 1996; **7**:293–301.
25. Keener J, Sneyd J. *Mathematical Physiology*. Springer Science and Business Media: New York, 2004.
26. Clayton RH, Panfilov AV. A guide to modelling cardiac electrical activity in anatomically detailed ventricles. *Progress in Biophysics and Molecular Biology* 2008; **96**:19–43.
27. Lafortune P, Aris R, Vazquez M, Houzeaux G. Coupled electromechanical model of the heart: parallel finite element formulation. *International Journal of Numerical Methods in Biomedical Engineering* 2012; **28**:72–86.
28. Rogers JM, McCulloch AD. A collocation-Galerkin finite element model of cardiac action potential propagation. *IEEE Transactions on Biomedical Engineering* 1994; **41**:743–757.
29. Böhl M, Abilez OJ, Assar AN, Zarins CK, Kuhl E. In vitro / in silico characterization of active and passive stresses in cardiac muscle. *International Journal for Multiscale Computational Engineering* 2012; **10**:171–188.
30. Pathmanathan P, Mirams GR, Southern J, Whiteley JP. The significant effect of the choice of ionic current integration method in cardiac electro-physiological simulations. *International Journal of Numerical Methods in Biomedical Engineering* 2011; **27**:1751–1770.
31. Keldermann RH, Nash MP, Panfilov AV. Pacemakers in a reaction-diffusion mechanics system. *Journal of Statistical Physics* 2007; **128**:375–392.
32. Land S, Niederer SA, Smith NP. Efficient computational methods for strongly coupled cardiac electromechanics. *IEEE Transactions on Biomedical Engineering* 2012; **59**:1219–1228.
33. Nordsletten DA, Niederer SA, Nash MP, Hunter PJ, Smith NP. Coupling multi-physics models to cardiac mechanics. *Progress in Biophysics and Molecular Biology* 2011; **104**:77–88.
34. Trayanova NA, Constantino J, Gurev V. Electromechanical models of the ventricles. *American Journal of Physiology-Heart and Circulatory Physiology* 2011; **301**:H279–H286.
35. Niederer SA, Smith NP. An improved numerical method for strong coupling of excitation and contraction models in the heart. *Progress in Biophysics and Molecular Biology* 2008; **96**:90–111.
36. Simo JC, Taylor RL. Consistent tangent operators for rate-independent elastoplasticity. *Computer Methods in Applied Mechanics and Engineering* 1985; **48**:101–118.
37. Taylor RL. *FEAP - A Finite Element Analysis Program*, Version 8.3, User Manual. University of California: Berkeley, 2011.
38. Göktepe S, Kuhl E. Computational modeling of electrophysiology: a novel finite element approach. *International Journal for Numerical Methods in Engineering* 2009; **79**:156–78.
39. Qu Z, Garfinkel A. An advanced algorithm for solving partial differential equations in cardiac conduction. *IEEE Transactions on Biomedical Engineering* 1999; **46**:1166–1168.
40. Wong J, Göktepe S, Kuhl E. Computational modeling of electrochemical coupling: a novel finite element approach towards ionic models for cardiac electrophysiology. *Computer Methods in Applied Mechanics and Engineering* 2011; **200**:3139–3158.
41. Hill A. The heat of shortening and the dynamic constants of muscle. *Proceedings of the Royal Society of London Series B* 1938; **126**:136–195.
42. Göktepe S, Kuhl E. Electromechanics of the heart - a unified approach to the strongly coupled excitation-contraction problem. *Computational Mechanics* 2010; **45**:227–243.

43. Dal H, Göktepe S, Kaliske M, Kuhl E. A fully implicit finite element method for bidomain models of cardiac electromechanics. *Computer Methods in Applied Mechanics and Engineering* 2013; **253**:323–336.
44. Luo CH, Rudy Y. A dynamic model of the cardiac ventricular action potential. I. Simulations of ionic currents and concentration changes. *Circulation Research* 1994; **74**:1071–1096.
45. Göktepe S, Acharya SNS, Wong J, Kuhl E. Computational modeling of passive myocardium. *International Journal of Numerical Methods in Biomedical Engineering* 2011; **27**:1–12.
46. Holzapfel GA, Ogden RW. Constitutive modelling of passive myocardium. A structurally-based framework for material characterization. *Philosophical Transactions of the Royal Society of London, Series A* 2009; **367**:3445–3475.
47. Rossi S, Ruiz-Baier R, Pavarino LF, Quarteroni A. Orthotropic active strain models for the numerical simulation of cardiac biomechanics. *International Journal of Numerical Methods in Biomedical Engineering* 2012; **28**:761–788.
48. Wang HM, Gao H, Luo XY, Berry C, Griffith BE, Ogden RW, Wang TJ. Structure-based finite strain modelling of the human left ventricle in diastole. *International Journal of Numerical Methods in Biomedical Engineering* 2013; **29**:83–103.
49. Yin FC, Chan CC, Judd RM. Compressibility of perfused passive myocardium. *American Journal of Physiology-Heart and Circulatory Physiology* 1996; **271**:1864–1870.
50. Cookson AN, Lee J, Michler C, Chabiniok R, Hyde E, Nordstletten DA, Sinclair M, Siebes M, Smith NP. A novel porous mechanical framework for modelling the interaction between coronary perfusion and myocardial mechanics. *Journal of Biomechanics* 2012; **45**:850–855.
51. Guccione JM, McCulloch AD. Mechanics of active contraction in cardiac muscle: Part I. Constitutive relations for active fiber stress that describe deactivation. *Journal of Biomechanical Engineering* 1993; **115**:72–81.
52. Rausch M, Dam A, Göktepe S, Abilez O, Kuhl E. Computational modeling of growth: systemic and pulmonary hypertension in the heart. *Biomechanics and Modeling in Mechanobiology* 2011; **10**:799–811.
53. Chapelle D, Gerbeau J-F, Sainte-Marie J, Vignon-Clementel IE. A poroelastic model valid in large strains with applications to perfusion in cardiac modeling. *Computational Mechanics* 2010; **101**:91–101.
54. Nash MP, Panfilov AV. Electromechanical model of excitable tissue to study reentrant cardiac arrhythmias. *Progress in Biophysics and Molecular Biology* 2004; **85**:501–522.
55. Hunter PJ, McCulloch AD, ter Kuers HEDJ. Modelling the mechanical properties of cardiac muscle. *Progress in Biophysics and Molecular Biology* 1998; **69**:289–331.
56. Ambrosi D, Arioli G, Nobile F, Quarteroni A. Electromechanical coupling in cardiac dynamics: the active strain approach. *SIAM Journal on Applied Mathematics* 2011; **71**:605–621.
57. Göktepe S, Menzel A, Kuhl E. Micro-structurally based kinematic approaches to electromechanics of the heart. In *Computer Models in Biomechanics*. Springer Science + Business Media: Dordrecht, 2013; 175–188.
58. ten Tusscher KHJ, Panfilov AV. Cell model for efficient simulation of wave propagation in human ventricular tissue under normal and pathological conditions. *Physics in Medicine and Biology* 2006; **51**:6141–6156.
59. Kotikanyadanam M, Göktepe S, Kuhl E. Computational modeling of electrocardiograms - a finite element approach towards cardiac excitation. *International Journal of Numerical Methods in Biomedical Engineering* 2010; **26**:524–533.
60. Wong J, Kuhl E. Generating fiber orientation maps in human heart models using Poisson interpolation. *Computer Methods in Biomechanics and Biomedical Engineering*. DOI: 10.1080/10255842.2012.739167. available online first.
61. Hurtado D, Kuhl E. Computational modeling of electrocardiograms: repolarization and T-wave polarity in the human heart. *Computer Methods in Biomechanics and Biomedical Engineering*. DOI: 10.1080/10255842.2012.729582. available online first.
62. Dokos S, Small BH, Young AA, LeGrice IJ. Shear properties of passive ventricular myocardium. *American Journal of Physiology-Heart and Circulatory Physiology* 2002; **283**:H2650–H2659.
63. Göktepe S, Wong J, Kuhl E. Atrial and ventricular fibrillation - computational simulation of spiral waves in cardiac tissue. *Archive of Applied Mechanics* 2010; **80**:569–580.
64. Moon MR, Ingels NB, Daughters GT, Stinson EB, Hansen DE, Miller DC. Alterations in left ventricular twist mechanics with inotropic stimulation and volume loading in human subjects. *Circulation* 1994; **89**:142–150.
65. Pathmanathan P, Chapman SJ, Gavaghan DJ, Whiteley JP. Cardiac electromechanics: the effect of contraction model on the mathematical problem and accuracy of the numerical scheme. *Quarterly Journal of Mechanics and Applied Mathematics* 2010; **63**:375–399.
66. Sainte-Marie J, Chapelle D, Cimrman R, Sorine M. Modeling and estimation of cardiac electromechanical activity. *Computers and Structures* 2006; **84**:1743–1759.
67. Sermesant M, Rhode K, Sanchez-Ortiz GI, Camara O, Andriantsimivona R, Hegde S, Rueckert D, Lambiase P, Bucknall C, Rosenthal E, Delingette H, Hill DLG, Ayache N, Razavi R. Simulation of cardiac pathologies using an electromechanical biventricular model and XMR interventional imaging. *Medical Image Analysis* 2005; **9**:467–480.
68. Böl M, Sturmat M, Weichert C, Kober C. A new approach for the validation of skeletal muscle modeling using MRI data. *Computational Mechanics* 2011; **47**:591–601.
69. Taylor CA, Figueroa CA. Patient-specific modeling of cardiovascular mechanics. *Annual Review of Biomedical Engineering* 2009; **11**:109–134.
70. Dal H, Göktepe S, Kaliske M, Kuhl E. A fully implicit finite element method for bidomain models of cardiac electrophysiology. *Computer Methods in Biomechanics and Biomedical Engineering* 2012; **15**:645–656.

71. Pathmanathan P, Bernabeu MO, Bordas R, Cooper J, Garny A, Pitt-Francis JM, Whiteley JP, Gavaghan DJ. A numerical guide to the solution of the bidomain equations of cardiac electrophysiology. *Progress in Biophysics and Molecular Biology* 2010; **102**:136–155.
72. Wong J, Abilez OJ, Kuhl E. Computational optogenetics - a novel continuum framework for the photoelectrochemistry of living systems. *Journal of the Mechanics and Physics of Solids* 2011; **200**:3139–3158.
73. Krittian SBS, Lamata P, Michler C, Nordsletten DA, Bock J, Bradley CP, Pitcher A, Kilner PJ, Markl M, Smith NP. A finite-element approach to the direct computation of relative cardiovascular pressure from time-resolved MR velocity data. *Medical Image Analysis* 2012; **16**:1029–1037.
74. Niederer SA, Kerfoot E, Benson AP, Bernabeu MO, Bernus O, Bradley C, Cherry EM, Clayton R, Fendton FH, Garny A, Heidenreich E, Land S, Maleckar M, Pathmanathan P, Plank G, Rodriguez JF, Roy I, Sachse FB, Seemann G, Skavhaug O, Smith NP. Verification of cardiac tissue electrophysiology simulators using an N-version benchmark. *Philosophical Transactions of the Royal Society of London, Series A* 2011; **369**:4331–4351.
75. Pathmanathan P, Bernabeu MO, Niederer SA, Gavaghan DJ, Kay D. Computational modeling of cardiac electrophysiology: explanation of the variability of results from different numerical solvers. *International Journal of Numerical Methods in Biomedical Engineering* 2012; **28**:890–903.
76. Greenstein JL, Winslow RL. An integrative model of the cardiac ventricular myocyte incorporating local control of Ca^{2+} release. *Biophysical Journal* 2002; **83**:2918–2945.
77. Priebe L, Beuckelmann DJ. Simulation study of cellular electric properties in heart failure. *Circulation Research* 1998; **82**:1206–1223.
78. ten Tusscher KHWJ, Bernus O, Hren R, Panfilov A. Comparison of electrophysiological models for human ventricular cells and tissues. *Progress in Biophysics and Molecular Biology* 2006; **90**:326–345.